Journal of Theoretical Biology 463 (2019) 138–154

Contents lists available at ScienceDirect

Journal of Theoretical Biology

journal homepage: www.elsevier.com/locate/jtb

Tumor growth and calcification in evolving microenvironmental geometries

Ying Chen[a], John S. Lowengrub[b,*]

[a] Department of Mathematics, Duke University, Durham, USA
[b] Department of Mathematics, Department of Biomedical Engineering, Center for Complex Biological Systems, University of California, Irvine, USA

ARTICLE INFO

Article history:
Received 30 April 2018
Revised 27 November 2018
Accepted 3 December 2018
Available online 5 December 2018

Keywords:
Tumor progression
Basement membrane
Dynamic geometry
Microcalcification
Ductal carcinoma in situ

ABSTRACT

In this paper, we apply the diffuse domain framework developed in Chen and Lowengrub (Tumor growth in complex, evolving microenvironmental geometries: A diffuse domain approach, J. Theor. Biol. 361 (2014) 14–30) to study the effects of a deformable basement membrane (BM) on the growth of a tumor in a confined, ductal geometry, such as ductal carcinoma in situ (DCIS). We use a continuum model of tumor microcalcification and investigate the tumor extent beyond the microcalcification. In order to solve the governing equations efficiently, we develop a stable nonlinear multigrid finite difference method. Two dimensional simulations are performed where the adhesion between tumor cells and the basement membrane is varied. Additional simulations considering the variation of duct radius and membrane stiffness are also conducted. The results demonstrate that enhanced membrane deformability promotes tumor growth and tumor calcification. When the duct radius is small, the cell-BM adhesion is weak or when the membrane is slightly deformed, the mammographic and pathologic tumor extents are linearly correlated, as predicted by Macklin et al. (J. Theor. Biol. 301 (2012) 122–140) using an agent-based model that does not account for the deformability of the basement membrane and the active forces that the membrane imparts on the tumor cells. Interestingly, we predict that when the duct radius is large, there is strong cell-BM adhesion or the membrane is highly deformed, the extents of the mammographic and pathologic tumors are instead quadratically correlated. The simulations can help surgeons to measure DCIS surgical margins while removing less non-cancerous tissue, and can improve targeting of intra- and post-operative radiotherapy.

© 2018 Elsevier Ltd. All rights reserved.

1. Introduction

Ductal carcinoma in situ (DCIS), the most common type of non-invasive breast cancer in women, is the first stage of breast cancer, in which tumor cells proliferate inside the milk duct or lobule. DCIS itself is not life-threatening, but if left untreated, DCIS may progress and a significant proportion of these tumors may evolve into invasive ductal carcinoma (Erbas et al., 2006; Kerlikowske et al., 2003; Page et al., 1982; Sakorafas and Tsiotou, 2000; Sanders et al., 2005). DCIS has four different morphological subtypes: micropapillary, cribriform, solid and comedo, and is typically diagnosed via microcalcifications in screening mammographies. Microcalcifications are produced when calcium is deposited in tumor cells that have died. Tumor cells may die for a variety of reasons including apoptosis and necrosis. When cells die, their surface receptors, e.g., E-cadherins and integrins, and subcellular structures degrade, the cell loses its liquid volume, and may eventually calcify (Panorchan et al., 2006). This calcified solid fraction can be detected by screening mammography. While much progress has been made, it is still problematic to detect how far the tumor extends from the microcalcification (Venkatesan et al., 2009). Better understanding of DCIS growth and calcification can help the radiologists to effectively use the mammograms and patient data to plan treatment.

Mathematical modeling and numerical simulations are essential for understanding and predicting the progression and dynamics of DCIS. Xu (2004) used the radially symmetric tumor growth model developed by Byrne and Chaplain (1995) to study spatial patterns (e.g., stripes, spots and uniform distributions) found in stationary solutions of the equations. In this model, tumor growth is governed by diffusion of cell substrates and the duct wall is assumed rigid; local pressure and cellular density are neglected. Franks et al. (2003a, 2003b, 2005) developed models that account for these effects, coupling existing models of avascular tumor growth with

* Corresponding author.
E-mail addresses: yingc@math.duke.edu (Y. Chen), lowengrb@math.uci.edu (J.S. Lowengrub).

https://doi.org/10.1016/j.jtbi.2018.12.006
0022-5193/© 2018 Elsevier Ltd. All rights reserved.

mechanical models for the finite deformation of a compliant basement membrane. The coupling was mediated by interactions between the expansive forces created by tumor cell proliferation and the stresses that develop in the basement membrane. Cell movement was described by a Stokes flow constitutive relation. The effects of the material properties (i.e., the viscosity) on the tumor shape, and the extent to which cells adhere to the duct wall were studied in Franks et al. (2003a). It was shown how stable, non-planar, interface configurations arise, and during the initial progression before the duct wall in breached, few cells die and a nutrient-rich model can be sufficient to capture the behavior. Franks et al. (2003b) further investigated the interactions between the expansive forces of cell proliferation and the stresses that develop in the compliant basement membrane. They showed how the duct wall deforms during tumor progression, and how tumor growth along the duct depends on wall stiffness.

Rejniak (2007a), Rejniak and Dillon (2007b), Rejniak and Anderson (2008a), Rejniak and Anderson (2008b) and Dillon et al. (2008) applied an immersed boundary method to a single-cell-based model, focusing on the biomechanical properties of individual cells and communication between cells and their microenvironment. Their models included a simplified description of the extracellular matrix (ECM) treated as viscous incompressible fluids and their models were able to reproduce several distinct microarchitectures of DCIS. Later, Norton et al. (2010) developed a 2D particle model of the growth of DCIS within a single breast duct considering mechanical effects such as cellular adhesion and intro-ductal pressure, and biological features including proliferation, apoptosis, necrosis, and cell polarity. They found that distinct morphological subtypes of DCIS could be generated by different regions of parameter space. A hybrid continuum-discrete model was recently developed to investigate the effect of interactions between tumor and stroma cells in DCIS and predicted the early stages of tumor invasion into stroma by incorporating breakdown of the epithelium into the model (Kim and Othmer, 2013). Gatenby et al. (2007), Smallbone et al. (2007), and Silva et al. (2010) developed the cellular automata models to investigate the role of hypoxia, glycolysis, and acidosis in DCIS evolution in 2D and 3D. Chapa et al. (2013) used an agent-based model to study the longitudinal pathogenesis of malignant transformation from normal mammary epithelium cells over a time period of 40 years by integrating extensive information based on cellular and molecular mechanisms in the pathogenesis of ductal epithelial breast cells. The authors mainly focused on the EGF and TGF-β signaling pathways and show the effects of up- or down-regulation of components in those pathways on cell growth and proliferation. The authors further considered an active motive force which is assumed to be generated by the cells at the leading edge of the invasive front, the chemical exchange of proteinases (MMPs) between tumor cells in the duct and fibroblasts/myofibroblasts in stromal tissue and the evolution of the extracellular matrix to model the collective migration of tumor cells that penetrate the basement membrane.

Macklin et al. (2012) developed a mechanistic, agent-based cell model of tumor growth in DCIS in which cell motion was determined by a balance of biomechanical forces. Each cell's phenotype was determined by genomic/proteomic- and microenvironment-dependent stochastic processes. The authors observed that the mammographic and pathologic sizes were linearly correlated and patient histopathology matched the predicted DCIS microstructure: an outer proliferation rim surrounds a stratified necrotic core with nuclear debris on its outer edge and calcification in the center. This work did not consider the deformability of the basement membrane or the active forces generated by stresses in the basement membrane. We consider these effects here in our model.

Very recently, Chen and Lowengrub (2014b) developed a mathematical model of tumor growth in complex, dynamic microenvironments with active, deformable membranes. Using a diffuse domain approach, the complex domain is captured implicitly using an auxiliary function and the governing equations are appropriately modified, extended and solved in a larger, regular domain. The boundary conditions appear as singular source terms in the reformulated equations. The diffuse domain method enables us to develop an efficient numerical implementation that does not depend on the space dimension or on the geometry of the microenvironment.

Chen and Lowengrub (2014b) applied this framework to a mixture model of tumor growth in duct-like geometries in two and three dimensions taking into account homotypic cell-cell adhesion and heterotypic cell-basement membrane (BM) adhesion with the latter being implemented via a membrane energy that models cell-BM interactions. The authors incorporated simple models of elastic forces generated in the BM and the degradation of the BM and ECM by tumor-secreted matrix degrading enzymes. They investigated tumor progression and BM response as a function of cell-BM adhesion and the stiffness of the BM finding that tumor sizes tend to be positively correlated with cell-BM adhesion since increasing cell-BM adhesion results in thinner, more elongated tumors that are easier for nutrients to penetrate. Prior to invasion of the tumor into the stroma, a negative correlation between tumor size and BM stiffness is found as the BM elastic restoring forces tend to inhibit tumor growth. However, a stiff BM was found to promote invasiveness because at early stages the opening in the BM created by MDE degradation from tumor cells tends to be narrower when the BM is stiffer. This requires invading cells to squeeze through the narrow opening and thus promotes fragmentation that then leads to enhanced growth and invasion.

In this paper, we extend the model of Chen and Lowengrub (2014b) to take into account tumor microcalcification. We do not consider tumor invasion here since we are modeling the early stages of breast tumors. This paper is organized as follows. In Section 2, we develop a mathematical model of tumor calcification in complex, evolving geometries using the diffuse domain approach. We briefly describe the numerical techniques and present two dimensional simulations in Section 3. Finally, In Section 4 we give some concluding remarks and discuss future work. The numerical method is described in the Appendix A.

2. Mathematical model

In this section, we present a mathematical model of tumor microcalcification in complex, dynamic geometries. We first, in Section 2.1, consider the case when a fixed (e.g., stationary), bounded, open tissue domain $\Omega \subset \mathbf{R}^d$, $d = 2$ or 3 contains the evolving tumor and membrane (e.g., see Fig. 1). Then, in Section 2.2 we extend the model to the case in which tumor growth is constrained by the membrane. Here we focus on $d = 2$ but the model straightforwardly extends to $d = 3$ (Chen and Lowengrub, 2014b). For the sake of clarity in the derivation below we indicate by **(Hyp.)** each hypothesis we make.

2.1. Modeling tumor growth and microcalcification using a mixture formulation

We begin by enumerating the key variables that describe the state of the system:

- ϕ_H, the volume fraction of the host tissue,
- ϕ_T, the volume fraction of the tumor cells,
- ϕ_V, the volume fraction of the viable tumor cells,
- ϕ_D, the volume fraction of the dead cells,

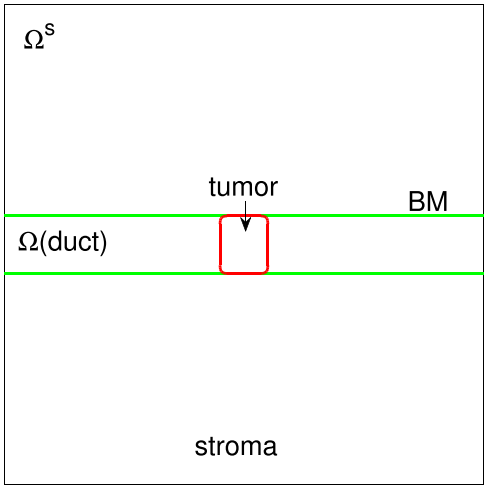

Fig. 1. Initial shape of tumor clusters (red, $\phi_T = 0.5$ contours) and basement membranes (green, $\psi = 0.5$ contours) used in the 2D simulations. (For interpretation of the references to colour in this figure legend, the reader is referred to the web version of this article.)

- ϕ_C, the volume fraction of the calcified cells,
- ϕ_W, the volume fraction of the water,
- $\mathbf{u}_S$, the mass-averaged cell velocity,
- $\mathbf{u}_W$, the interstitial fluid velocity,
- p, the solid pressure,
- q, the interstitial fluid pressure,
- n, the nutrient concentration.

We assume that there are no voids (i.e., the mixture is saturated) and thus

$$\phi_H + \phi_T + \phi_W = 1, \tag{1}$$

where $\phi_T = \phi_V + \phi_D + \phi_C$. **(Hyp. 1)** We follow Wise et al. (2008) and for simplicity, we assume (i) the densities of each component are matched and (ii) $\phi_W = \bar{\phi}_W$ constant, so that $\phi_S = \phi_H + \phi_T = \bar{\phi}_S = 1 - \bar{\phi}_W$. The latter enables us to partially decouple the solid and liquid components and recent results indicate that the overall behavior of the system is similar even when the solid and liquid fractions vary (Thomas, 2017). Rescaling the solid volume fractions by $\bar{\phi}_S$, (e.g., $\tilde{\phi}_T = \phi_T/\bar{\phi}_S$, etc) and the liquid fraction by $\bar{\phi}_W$ we obtain $\tilde{\phi}_H + \tilde{\phi}_T = 1$ and $\tilde{\phi}_W = \phi_W/\bar{\phi}_W = 1$. Hereafter we drop the tilde notation. The volume fractions of the components are assumed to be continuous in Ω, which contains both the tumor and host domains. The volume fractions obey the mass conservation equations

$$\frac{\partial \phi_i}{\partial t} + \nabla \cdot (\mathbf{u}_i \phi_i) = -\nabla \cdot \mathbf{J}_i + S_i \quad \text{in} \quad \Omega, \tag{2}$$

where $i = H,\ V,\ D,\ C,\ W$ denotes the component, $\mathbf{J}_i$ are fluxes, $\mathbf{u}_i$ are velocities of each component, and S_i are source terms that account for intercomponent mass exchange as well as gains due to cell proliferation and loss due to cell death. Constitutive laws for these quantities will be given below. Note the fluxes and source terms have been rescaled by the densities. **(Hyp. 2)** Following Wise et al. (2008), we assume that cells are tightly packed and they march together. Consequently, all cells move with the mass-averaged velocity $\mathbf{u}_S$, e.g., $\mathbf{u}_T = \mathbf{u}_D = \mathbf{u}_V = \mathbf{u}_C = \mathbf{u}_H = \mathbf{u}_S$. Constitutive laws for $\mathbf{J}_i$ and the velocities $\mathbf{u}_S$ and $\mathbf{u}_W$ will be derived below using a variational energy argument in an Eulerian (e.g., laboratory) frame. Mass conservation of the mixture implies $\sum_i \mathbf{J}_i = 0$ and $\sum_i S_i = 0$ (e.g., sum Eq. (2) over i). Note this implies that $S_W = -(S_T + S_H)$ where $S_T = S_V + S_D$. **(Hyp. 3)** We next assume that (i) on the time scales considered that there is no proliferation or death of the host tissue $S_H = 0$ and (ii) that $\mathbf{J}_W = \mathbf{0}$ so that the movement of water is solely due to the source S_V and to the velocity $\mathbf{u}_W$. This implies that the sum of the fluxes of the solid fractions $\mathbf{J}_T = -\mathbf{J}_H$ and that $S_W = -S_T$.

In order to determine the fluxes $\mathbf{J}_i$ and the velocities $\mathbf{u}_S$ and $\mathbf{u}_W$ in Eq. (2), we use an energy variational argument (Chen et al., 2014a; Wise et al., 2008). **(Hyp. 4)** Following these references, we assume that there is energy associated with the tumor/host interface (e.g., because there are differences between the adhesiveness of the tumor and host cells). This can be implemented via (Wise et al., 2008)

$$E_{ad} = \frac{\gamma}{\epsilon} \int_\Omega f(\phi_T) + \frac{\epsilon^2}{2} |\nabla \phi_T|^2 d\mathbf{x}, \tag{3}$$

where γ and ϵ are parameters that reflect the strength of the energy and the penalty for the presence of gradients in ϕ_T, respectively. We can interpret this energy as $E_{ad} = \sum_{i=H,V,D,C} E_{ad,i}$ where $E_{ad,i} = \frac{\gamma_i}{\epsilon_i} \int_\Omega f_i + \frac{\epsilon_i^2}{2} |\nabla \phi_i|^2 d\mathbf{x}$ and we have taken $\gamma_i = \gamma$, $\epsilon_i = \epsilon$, and $f_i = f(\phi_T)$. **(Hyp. 5)** Assuming $f(\phi) = \frac{1}{4}\phi^2(1-\phi)^2$, which is a double-well bulk energy, the energy (3) favors the separation of space into regions containing nearly all tumor cells $\phi_T \approx 1$ and those containing nearly all host tissue $\phi_H = 1 - \phi_T = 1$ with these regions being separated by an interface with thickness proportional to ϵ (see Pego, 1989; Wise et al., 2008). This is a diffuse-interface representation of the tumor-host interfacial energy. Further, E_{ad} mimics cell-cell adhesion and its form implies that it does not account for differences in the adhesiveness of the different tumor components but that the tumor cells prefer to adhere to one another rather than the host tissue. The $1/\epsilon$ scaling ensures that in the limit as $\epsilon \to 0$, E_{ad} converges to a finite limit that is proportional to the interface length. **(Hyp. 6)** To account for the presence of the calcified cells, we assume that rather than being dispersed throughout the tumor, the calcified cells tend to form a solid-like mass within the tumor, as observed in experiments. Accordingly, we assume that there is also energy associated with the interface between solid-like regions of calcified cells and the rest of the tumor. By analogy with the tumor-host interface, this can be implemented as:

$$E_{cad} = \frac{\gamma_C}{\bar{\epsilon}} \int_\Omega f(\phi_C) + \frac{\bar{\epsilon}^2}{2} |\nabla \phi_C|^2 d\mathbf{x}, \tag{4}$$

where γ_C is the strength of the energy and f is the same double-well energy as used above. This energy favors the separation of the tumor domain into regions containing nearly all calcified cells ($\phi_C \approx 1$, $\phi_T \approx 1$) separated from the rest of the tumor ($\phi_C \approx 0$, $\phi_T \approx 1$) by a diffuse interface with thickness proportional to $\bar{\epsilon}$. As with the adhesion energy, the E_{cad} can be written as a sum of appropriate energies of the individual components. **(Hyp. 7)** To account for the basement membrane, we follow Chen et al. (2014a) in which we developed a simple model to simulate the effect of an embedded deformable elastic membrane. We modeled the membrane using an auxiliary function $\psi(x, t)$, e.g. $\psi(x, t) = 1/2$ implicitly defines the membrane location at time t, and a simplified form of the elastic energy E_{el} was given by

$$E_{el} = \frac{A}{2} \int_\Omega \left(\psi - \Psi\right)^2 d\mathbf{x}, \tag{5}$$

where Ψ is the reference state of the membrane taken to be its initial value $\Psi = \psi(\mathbf{x}, 0)$, and A represents the stiffness of the membrane (e.g., a simplified version of Hooke's law). Accounting for all these sources of energy, we take the energy of the mixture to be

$$E = E_{ad} + E_{cad} + E_{el}. \tag{6}$$

Note that the presence of ϕ_C in E_{ad} (through ϕ_T) and in E_{el} merely reflects the fact that there is energy associated with both the tumor/host interface and the interface surrounding the solid-like regions of calcified cells.

Next, taking the time derivative of the energy, we obtain

$$\frac{dE}{dt} = \frac{\gamma}{\epsilon}\int_\Omega \frac{\partial \phi_T}{\partial t}\mu \, d\mathbf{x} + \frac{\gamma_C}{\bar{\epsilon}}\int_\Omega \frac{\partial \phi_C}{\partial t}\mu_C \, d\mathbf{x} + A\int_\Omega (\psi - \Psi)\frac{\partial \psi}{\partial t} \, d\mathbf{x}, \tag{7}$$

where we have integrated by parts and **(Hyp. 8)** assumed zero Neumann boundary conditions $\mathbf{n}\cdot\nabla\phi_T = \mathbf{n}\cdot\nabla\phi_C = 0$ on $\partial\Omega$, where $\mathbf{n}$ is the outward normal vector to $\partial\Omega$. While $\frac{\partial\phi_T}{\partial t}$ contains $\frac{\partial\phi_C}{\partial t}$, we keep these terms separate as in the end we solve equations for ϕ_T, ϕ_C, ϕ_D and infer $\phi_V = \phi_T - (\phi_C + \phi_D)$ and $\phi_H = 1 - \phi_T$. The Neumann boundary conditions imply that if the tumor (and calcified region) intersects $\partial\Omega$ then the contact angle is 90° (Chen and Lowengrub, 2014b). However, in the simulations presented below, we stop before the tumor hits $\partial\Omega$. The functions (chemical potentials) μ and μ_C are given by

$$\mu = f'(\phi_T) - \epsilon^2\nabla^2\phi_T, \tag{8}$$

and

$$\mu_C = f'(\phi_C) - \bar{\epsilon}^2\nabla^2\phi_C. \tag{9}$$

To determine the constitutive laws for $\mathbf{J}_i$, $\mathbf{u}_S$ and $\mathbf{u}_W$ we follow Wise et al. (2008) and ask **(Hyp. 9)** that the system (free) energy E decreases in time in the absence of mass sources/sinks (e.g., a closed system). In particular, we set the source terms $S_i = 0$ to derive the constitutive laws. Later, when we simulate the system with $S_i \neq 0$, we use the same constitutive laws even though the free energy may not decrease because of external influences (e.g., nutrient delivery) that drive mass changes (e.g., an open system). Next, **(Hyp. 10)** assuming the membrane moves with the cell velocity (Chen et al., 2014a)

$$\frac{\partial\psi}{\partial t} + \mathbf{u}_S\cdot\nabla\psi = 0, \tag{10}$$

and using Eq. (2), with the source terms $S_i = 0$, in Eq. (7), we obtain

$$\begin{aligned}\frac{dE}{dt} &= \frac{\gamma}{\epsilon}\int_\Omega (\mathbf{J}_T + \mathbf{u}_s\phi_T)\cdot\nabla\mu \, d\mathbf{x} + \frac{\gamma_C}{\bar{\epsilon}}\int_\Omega (\mathbf{J}_C + \mathbf{u}_s\phi_C)\cdot\nabla\mu_C \, d\mathbf{x} \\ &\quad - A\int_\Omega \mathbf{u}_s\cdot(\psi - \Psi)\nabla\psi \, d\mathbf{x} \\ &= \frac{\gamma}{\epsilon}\int_\Omega \mathbf{J}_T\cdot\nabla\mu \, d\mathbf{x} + \frac{\gamma_C}{\bar{\epsilon}}\int_\Omega \mathbf{J}_C\cdot\nabla\mu_C \, d\mathbf{x} \\ &\quad + \int_\Omega \mathbf{u}_s\cdot\left(\frac{\gamma}{\epsilon}\phi_T\nabla\mu + \frac{\gamma_C}{\bar{\epsilon}}\phi_C\nabla\mu_C - A(\psi - \Psi)\nabla\psi\right) d\mathbf{x}.\end{aligned} \tag{11}$$

(Hyp. 11) Assuming that each term should dissipate energy, then we may take the fluxes and velocity to be:

$$\mathbf{J}_T = -M\phi_T\nabla\mu, \quad \mathbf{J}_C = -\bar{M}\phi_C\nabla\mu_C, \tag{12}$$

$$\mathbf{u}_S = -M_S\left(\nabla p + \frac{\gamma}{\epsilon}\phi_T\nabla\mu + \frac{\gamma_C}{\bar{\epsilon}}\phi_C\nabla\mu_C - A(\psi - \Psi)\nabla\psi\right), \tag{13}$$

although other choices are possible (e.g., there could be cross-diffusion or Stokes flow could be used instead of Darcy's law in Eq. (13)). Here, p is a pressure that arises from the constraint that the solid fraction is constant. In the derivation here, since we have taken $S_i = 0$ it follows that $\nabla\cdot\mathbf{u}_S = 0$ (e.g., sum Eq. (2) over $i = H, V, D, C$). Further, M, $\bar{M}$ are mobilities and M_S is a generalized permeability, all of which are **(Hyp. 12)** assumed to be constant, which reflects the fact that corresponding cells respond equally to the driving forces (e.g., gradients of the chemical potentials, pressure). Taking $\bar{M} < M$ implies that the calcified cells are less mobile than the other tumor components. With these choices and **(Hyp. 13)** using the natural boundary conditions $\mathbf{u}\cdot\mathbf{n} = 0$ (e.g., $\phi_T\nabla\mu\cdot\mathbf{n} = 0 = \phi_C\nabla\mu_C\cdot\mathbf{n}$ and $(\nabla p - A(\psi - \Psi)\nabla\psi)\cdot\mathbf{n} = 0$), which implies that the tumor does not flux out of the domain, we obtain

$$\begin{aligned}\dot{E} &= -\frac{\gamma}{\epsilon}\int_\Omega M\phi_T|\nabla\mu|^2 \, d\mathbf{x} - \frac{\gamma_C}{\bar{\epsilon}}\int_\Omega \bar{M}\phi_C|\nabla\mu_C|^2 \, d\mathbf{x} \\ &\quad - \int_\Omega \frac{1}{M_S}|\mathbf{u}_S|^2 \, d\mathbf{x}.\end{aligned} \tag{14}$$

Now, recall that $\phi_T = \phi_V + \phi_D + \phi_C$, so that we may only solve Eq. (2) for three of the four volume fractions ϕ_T, ϕ_V, ϕ_D and ϕ_C. Following previous work (Chen et al., 2014a; Wise et al., 2008), we solve Eq. (2) for ϕ_D, ϕ_C and ϕ_T and infer $\phi_V = \phi_T - (\phi_D + \phi_C)$. **(Hyp. 14)** We will assume that the flux for ϕ_D is

$$\mathbf{J}_D = -\hat{M}\phi_D\nabla\mu, \tag{15}$$

where $\hat{M}$ is the mobility of the dead cells, which is introduced to account for the fact that the dead cells may be less mobile than the viable cells. Since $\mathbf{J}_T = \mathbf{J}_V + \mathbf{J}_D + \mathbf{J}_C$, we obtain

$$\mathbf{J}_V = -M\phi_V\nabla\mu - \left(M - \hat{M}\right)\phi_D\nabla\mu - \phi_C\nabla\left(M\mu - \bar{M}\mu_C\right). \tag{16}$$

Note that this is different from what we assumed before in previous work. In particular, the second and third terms on the right hand side of Eq. (16) did not appear in Wise et al. (2008) or Chen et al. (2014a). These terms arise from the different mobilities and fluxes of the components. Nevertheless, we expect these terms to be small. As discussed in Pego (1989) and Wise et al. (2008), the gradient terms $\nabla\mu$ and $\nabla\mu_C$ are only non-zero near the tumor/host and calcified cell interfaces, respectively. Near these interfaces, analysis shows that these terms are $O(\epsilon)$ and $O(\bar{\epsilon})$, respectively. Therefore, $\mathbf{J}_V \approx -M\phi_V\nabla\mu + O(\epsilon)$. However, since we never solve Eq. (2) for ϕ_V, $\mathbf{J}_V$ is never actually used in the model.

Finally, using the advection Eq. (10) for the membrane ψ may introduce numerical instabilities due to contour bunching and the formation of large gradients due to local compression and expansion. Therefore, **(Hyp. 15)** we use an advective Cahn–Hillard equation for the dynamics instead. Here, the Cahn–Hillard part of the equation should be thought of as a regularization of advection and does not directly follow from the system energy. A similar approach was used previously in Chen et al. (2014a). As a result, the transport of ψ is as follows

$$\frac{\partial\psi}{\partial t} = \nabla\cdot(\tilde{M}(\psi)\nabla\tilde{\mu}) - \mathbf{u}_S\cdot\nabla\psi, \tag{17}$$

$$\tilde{\mu} = f'(\psi) - \tilde{\epsilon}^2\nabla^2\psi. \tag{18}$$

Because the membrane has co-dimension 1 (e.g., a curve in $2D$) we follow previous work (e.g., Aland et al., 2014; Chen et al., 2014a) and assume **(Hyp. 16)** that the mobility $\tilde{M}(\psi)$ is localized near the interface $\psi \approx 1/2$, e.g., $\tilde{M}(\psi) = 4\tilde{M}\psi^2(1-\psi)^2$ to limit the dynamics of ψ to the region around the membrane. Because this system rapidly equilibrates near the interface, analysis (Lowengrub and Truskinovsky, 1998; Aland et al., 2014) shows that $\nabla\cdot\left(\tilde{M}(\psi)\nabla\tilde{\mu}\right) = O(\tilde{\epsilon})$. When $\tilde{\epsilon}$ is small, its effects are limited to preventing contours of the solution from bunching across the interface, which maintains a uniform thickness of the interface along the duct.

We assume **(Hyp. 17)** that the net source of viable tumor cells S_V is

$$S_V = \lambda_M n\phi_V - \lambda_A\phi_V - \lambda_N\mathscr{H}(n_N - n)\phi_V, \tag{19}$$

where the parameters λ_M, λ_A and λ_N are the mitosis, apoptosis and necrosis rates of tumor cells, respectively. $\mathscr{H}$ is a Heaviside step function. It is assumed **(Hyp. 18)** that viable tumor cells necrose based on the level of the local nutrient concentration n, i.e., when the nutrient level is below the cell viability limit n_N, cells die. Assume **(Hyp. 19)** that the net source of dead cells S_D is

$$S_D = \lambda_A\phi_V + \lambda_N\mathscr{H}(n_N - n)\phi_V - \lambda_L\phi_D - \lambda_C\phi_D, \tag{20}$$

where λ_L and λ_C are the lysing and calcification rates of dead cells, respectively. The net source of calcified cells is assumed **(Hyp. 20)** to be

$$S_C = \lambda_C \phi_D - \lambda_{LC} \phi_C, \tag{21}$$

where λ_{LC} is degradation rate of the calcified cells. Macklin et al. (2012) predict that the proliferative rim and necrotic core are mechanically separated by a small gap, which occurs from the mechanics of necrotic cell swelling and fast lysis. our model here doesn't consider necrotic cell swelling, but it could be straightforwardly extended to include this effect by introducing another population of cells – swelling necrotic cells that then eventually degrade once they get too big and burst.

Assuming **(Hyp. 21)** that there is no proliferation or death of the host tissue, the velocity is constrained to satisfy

$$\nabla \cdot \mathbf{u}_S = S_T, \tag{22}$$

which yields a Poisson equation for the pressure

$$-\Delta p = S_T + \frac{\gamma}{\epsilon}\nabla(\phi_T \nabla \mu) + \frac{\gamma_C}{\bar{\epsilon}}\nabla(\phi_C \nabla \mu_C) - A\nabla(\psi \nabla(\Psi - \psi)), \tag{23}$$

where S_T is the sum of S_V, S_D and S_C, i.e.,

$$S_T = \lambda_M n \phi_V - \lambda_L \phi_D - \lambda_{LC} \phi_C. \tag{24}$$

Next, we briefly discuss the dynamics of the water. Because we have assumed ϕ_W is constant (scaled to 1), $\mathbf{J_W} = 0$, and $S_H = 0$, Eq. (2) for the water component becomes $\nabla \cdot \mathbf{u}_W = S_W = -S_T$. To complete the description, **(Hyp. 22)** we assume that the motion of the water is given by Darcy's law $\mathbf{u}_W = -M_W \nabla q$, where q is the interstitial fluid pressure. Mass conservation requires that $\nabla \cdot (\mathbf{u}_S + \mathbf{u}_W) = 0$ (recall that we have rescaled the constant liquid and solid volume fractions to one), which relates the solid and interstitial pressures by $\nabla \cdot (M_S \nabla p + M_W \nabla q) = 0$. In the following, we do not track the dynamics of the liquid component; its dynamics is solely determined by that of the tumor components.

The nutrient diffuses through interstitial fluid to reach all cells. For simplicity, we here model the host tissue at equilibrium. **(Hyp. 23)** Whatever nutrient is uptaken by the host tissue is assumed to be replaced by supply from the normal vasculature. However, in the tumor, not only the nutrient uptake of the tumor cells in general greatly exceeds the supply, but also can be much higher than that of the host tissue. Moreover, over the proliferation time scales, the diffusive transport of nutrient dominates that from fluid transport so that the nutrient equation is quasi-steady **(Hyp. 24)**. This is because diffusion occurs over much shorter time scales (e.g. minute) than does cell proliferation (e.g. day or more) so that the nutrient field rapidly equilibrates, see Wise et al. (2008). The nutrient is proposed to evolve quasi-statically and satisfies

$$0 = \nabla \cdot (D(\phi_T)\nabla n) + T_C(\phi_T, n) - \nu_U n \phi_V, \tag{25}$$

where the term $D(\phi_T)$ is the nutrient diffusion coefficient, which may be different in the tumor and host domains. The term $T_C(\phi_T, n)$ represents the nutrient source from the vasculature defined below in Eq. (43).

2.2. Diffuse domain formulation

We next extend the model by **(Hyp. 25)** assuming that the basement membrane (BM) bounds the domain where the tumor is growing (Fig. 1). Further, we explicitly account for cell-BM adhesion. We model the cell-BM adhesive energy as (Chen and Lowengrub, 2014b; Jacqmin, 1999),

$$E_m = \int_{\Gamma_{BM}} g(\phi_T) \mathrm{d}s, \tag{26}$$

where $g(\phi_T)$ is an energy density and Γ_{BM} denotes the BM. A variational argument shows that this introduces the boundary condition (Granasy et al., 2007):

$$\frac{1}{\epsilon^2} g'(\phi_T) = -\nabla \phi_T \cdot \hat{\mathbf{n}}. \tag{27}$$

Taking $g(\phi_T) = \frac{\epsilon}{\sqrt{2}}(\frac{\phi_T^2}{2} - \frac{\phi_T^3}{3})\cos(\theta)$, where θ models the static contact angle (e.g., Aland et al., 2010; Do-Quang and Amberg, 2010; Granasy et al., 2007; Jacqmin, 1999; Teigen et al., 2009; Teigen et al., 2011), that reflects the difference in cell-cell, cell-ECM, and ECM-ECM adhesion energies. This is analogous with Young's relation for multicomponent fluids. When $\theta < 90^o$ tumor cells prefer to adhere to each other than to the BM while the converse is true when $\theta > 90^o$.

We consider a complex, dynamic tumor and host domain Ω (Fig. 1), which is represented by a phase field function ψ and is contained in a large, fixed (e.g., stationary) regular domain Ω^s. The phase field function ψ approximates the characteristic function of the domain Ω such that $\psi \approx 1$ in Ω and $\psi \approx 0$ in Ω^s/Ω. The boundary $\partial\Omega$, which may be time-dependent, is described implicitly using the set $\partial\Omega(t) = \{\mathbf{x} | \psi(\mathbf{x}, t) = 1/2\}$.

We next reformulate Eq. (2) and the boundary conditions on $\partial\Omega$ using the diffuse domain formulation (Aland et al., 2010; Chen and Lowengrub, 2014b; Li et al., 2009; Teigen et al., 2009; 2011) where the equations are extended into Ω^S and the boundary conditions are incorporated as singular source terms. Accordingly, we obtain

$$\frac{\partial(\psi\phi_i)}{\partial t} + \nabla \cdot (\psi \mathbf{u}_i \phi_i) = -\nabla \cdot (\psi \mathbf{J}_i) + \psi S_i \quad \text{in} \quad \Omega^s, \tag{28}$$

where we have **(Hyp. 26)** assumed no-flux boundary conditions $\mathbf{J}_i \cdot \mathbf{n} = 0$ on $\partial\Omega$ because the surface moves with the cells. To determine the fluxes $\mathbf{J}_i$ and the velocities $\mathbf{u}_i$ in Eq. (28), we use an energy variation argument analogous to that in the previous subsection to derive the constitutive laws, which is consistent with a dissipative biophysical energy.

In the following we reformulate the tumor cell-cell adhesion energy Eq. (6) and calcified cell-cell adhesion energy Eq. (4) in the large domain Ω^s as

$$\tilde{E}_{ad} = \frac{\gamma}{\epsilon}\int_{\Omega^s} \psi \ (f(\phi_T) + \frac{\epsilon^2}{2}|\nabla \phi_T|^2)\mathrm{d}\mathbf{x}, \tag{29}$$

$$\tilde{E}_{cad} = \frac{\gamma_C}{\bar{\epsilon}}\int_{\Omega^s} \psi (f(\phi_C) + \frac{\bar{\epsilon}^2}{2}|\nabla \phi_C|^2)\mathrm{d}\mathbf{x}, \tag{30}$$

and use a surface delta function δ_Γ to rewrite the cell-membrane interaction forces in the domain Ω^s

$$\tilde{E}_m = \frac{\gamma}{\epsilon}\int_{\Omega^s} \delta_\Gamma g(\phi_T)\mathrm{d}\mathbf{x}, \tag{31}$$

where $\Gamma = \partial\Omega$ and we take $\delta_\Gamma \approx \frac{\epsilon}{2}|\nabla\psi|^2$ as a diffuse interface approximation of the surface delta function, with ϵ characterizing the width of the diffuse boundary of the domain Ω. All together, the total free energy of the system becomes

$$E_{total} = \tilde{E}_{ad} + \tilde{E}_{cad} + \tilde{E}_m + E_{el}. \tag{32}$$

A variational argument gives that

$$\psi\mu = \psi f'(\phi_T) - \epsilon^2 \nabla \cdot (\psi \nabla \phi_T) + \epsilon g'(\phi_T)|\nabla\psi|, \tag{33}$$

where the term $\epsilon g'(\phi_T)|\nabla\psi|$ comes from the diffuse domain approximation of the tumor-membrane boundary condition (27).

Correspondingly, a generalized Darcy's law gives

$$\mathbf{u}_S = -\nabla \hat{p} - \frac{\hat{\gamma}}{\epsilon}\psi\phi_T\nabla\mu - \frac{\hat{\gamma}_c}{\bar{\epsilon}}\psi\phi_C\nabla\mu_C + \hat{A}\psi\nabla(\Psi - \psi) + \mathbf{v}, \tag{34}$$

where we have incorporated the permeability M_S into the modified pressure: $\hat{p} = M_S(p + A(\psi - \Psi)\psi)$ and energies $\hat{\gamma} = M_S\gamma$, $\hat{\gamma}_C = M_S\gamma_C$ and $\hat{A} = M_S A$. Further,

$$\mathbf{v} = \frac{\hat{\gamma}}{\epsilon}\left(\phi_T\mu - (f(\phi_T) + \frac{\epsilon^2}{2}|\nabla\phi_T|^2)\right)\nabla\psi - \delta_\Gamma\nabla g(\phi_T).$$

The term $\delta_\Gamma\nabla g(\phi_T)$ comes from the active tumor-membrane boundary, and other terms on the right hand side of $\mathbf{v}$ equation come from the cell-cell adhesion. In the remainder of the paper, we use the modified pressure and drop the hat notation.

Substituting the fluxes $\mathbf{J}_i$ and the velocity $\mathbf{u}_S$ into Eq. (28), the tumor volume fraction ϕ_T follows a Cahn–Hilliard-type advection-reaction-diffusion equation

$$\frac{\partial(\psi\phi_T)}{\partial t} = \nabla\cdot(M\psi\phi_T\nabla\mu) + \psi S_T - \nabla\cdot(\psi\phi_T\mathbf{u}_S), \tag{35}$$

where $M > 0$ represents the diffusive mobility of the tumor cells. Rather than solving for the volume fraction of viable tumor cells ϕ_V, a dynamic equation for the volume fraction of dead cells ϕ_D is used instead

$$\frac{\partial(\psi\phi_D)}{\partial t} = \nabla\cdot(\bar{M}\psi\phi_D\nabla\mu) + \psi S_D - \nabla\cdot(\psi\phi_D\mathbf{u}_S). \tag{36}$$

The calcified cell volume fraction ϕ_C follows

$$\frac{\partial(\psi\phi_C)}{\partial t} = \nabla\cdot(\bar{M}\psi\phi_C\nabla\mu_C) + \psi S_C - \nabla\cdot(\psi\phi_C\mathbf{u}_S), \tag{37}$$

with μ_C satisfying

$$\psi\mu_C = \psi f'(\phi_C) - \bar{\epsilon}^2\nabla\cdot(\psi\nabla\phi_C). \tag{38}$$

Knowing ϕ_T, ϕ_D, and ϕ_C , the volume fraction of viable tumor cells is calculated as $\phi_V = \phi_T - \phi_D - \phi_C$, and the volume fraction of the host cells is recovered as $\phi_H = 1 - \phi_T$.

Since we have assumed that ϕ_W remains constant and that there is no proliferation and death of the host tissue, the velocity is constrained to satisfy

$$\nabla\cdot\mathbf{u}_S = \frac{\psi}{\psi + \bar{\delta}}S_T, \tag{39}$$

where $\bar{\delta}$ is a small positive number.

Together, Eqs. (34) and (39) constitute a Poisson equation for the solid pressure p:

$$-\Delta p = \frac{\gamma}{\epsilon}\nabla\cdot(\phi_T\psi\nabla\mu) + \frac{\gamma_c}{\bar{\epsilon}}\nabla \cdot(\phi_C\psi\nabla\mu_C) - A\nabla\cdot(\psi\nabla(\Psi - \psi)) - \nabla\cdot\mathbf{v} + \frac{\psi}{\psi + \bar{\delta}}S_T. \tag{40}$$

The Quasi-steady nutrient equation is given by

$$0 = \nabla\cdot(D(\psi\phi_T)\nabla n) + T_C(\psi\phi_T, n) - \psi\nu_U n\phi_V. \tag{41}$$

The diffusion coefficient $D(\phi_T)$ and nutrient capillary source term $T_C(\psi\phi_T, n)$ are

$$D(\psi\phi_T) = D_H(1 - Q(\psi\phi_T)) + D_T Q(\psi\phi_T), \tag{42}$$

$$T_C(\psi\phi_T, n) = (\nu_P^H(1 - Q(\psi\phi_T)) + \nu_P^T Q(\psi\phi_T))(n_C - n), \tag{43}$$

where D_H is the nutrient diffusion coefficient in the host domain, ν_P^H and ν_P^T denote the nutrient transfer rates for pre-existing vasculature in the tumor and host domains, and n_C is the nutrient level in the capillaries. The function $Q(\phi)$ is used to interpolate between the tumor and host tissue, and is defined as

$$Q(\phi) = \begin{cases} 1 & \text{if } 1 \le \phi \\ \phi & \text{if } 0 < \phi < 1 \\ 0 & \text{if } \phi \le 0. \end{cases}$$

For simplicity, we take $D_H = D_T$ here.

Eqs. (35)–(41) and (17)–(18) are valid on the extended domain Ω^s and not just in the tumor volume Ω_T. To complete the system we choose the following boundary conditions **(Hyp. 27)**

$$\mathbf{n}\cdot\nabla\phi_T = \mathbf{n}\cdot\nabla\phi_D = \mathbf{n}\cdot\nabla\phi_C = \mathbf{n}\cdot\nabla\psi = p = q = \mu = \mu_C = \tilde{\mu} = 0, \quad n = 1 \quad \text{on } \partial\Omega^s.$$

As long as the tumor does not intersect the boundary of the extended domain Ω^s, the results are insensitive to the choice of boundary conditions on $\partial\Omega^s$.

3. Numerical results

In order to numerically solve the governing system of equations derived in the previous section, a stable numerical scheme developed in Chen and Lowengrub (2014b); Chen et al. (2014a) is used to solve the equations. The numerical method used here is stable, but not energy stable since the overall formulation is not fully variational. Adaptive, block-structured Cartesian mesh refinement is used to increase accuracy locally (Wise et al., 2011). The details of the algorithm are given in the Appendix A. The equations are solved in nondimensional form using the diffusion length $l = \sqrt{D/\nu_U}$ and a characteristic cell division time $\tau = \lambda_M^{-1}$. The nondimensional model takes the same form as the dimensional version; the nondimensional parameters are given in Table 1.

We consider a simple duct geometry as shown in Fig. 1. The red curves correspond to the tumor boundaries ($\phi_T = 0.5$) while the green curves denote the basement membrane ($\psi = 0.5$).

Initially small clusters of tumor cells occupy the whole diameter of the ductal membrane with a subset of tumor clusters attached to the BM. We do not explicitly model the layer of normal epithelial cells (ECs) that are also attached to the BM (away from the tumor), but the model could be straightforwardly extended to this case. We instead assume that the normal ECs are displaced by the growing tumor. We do not model the thickness of the BM and we assume that the tumor has grown across the lumen. We also assume that the tumors are avascular with nutrients supplied by diffusion from a pre-existing vasculature in the stroma by taking the nutrient capillary source term in Eq. (43) to be $T_C = \nu_P^H(1 - Q(\psi\phi_T))(n_C - n)$. See Table 1 for the values of the nondimensional parameters.

We begin by investigating how the cell-membrane adhesion affects tumor growth and calcification. In particular, we vary the cell-membrane contact angle θ and investigate the evolution of the small tumor clusters. Recall that a small value of θ (e.g., $\theta < 90°$) implies that tumor cells strongly prefer to adhere to each other rather than to the BM. A large value of θ (e.g., $\theta > 90°$) corresponds to the case in which tumor cells prefer to adhere to the BM. In Fig. 2, characteristic tumor-BM evolutions are shown at different times (columns) for different contact angles (rows; [a]: 30°, [b]: 90°, [c]: 120°, [d]: 150°, [e]: 180°). The locations of the tumor boundaries (red, $\phi_T = 0.5$ contour), calcified cells (magenta, $\phi_C = 0.5$ contour), necrotic cores (white) and BM (green, $\psi = 0.5$ contour) are shown in Fig. 2. As the tumors grow along the BM, the deformation of the membrane is driven by the proliferation of the tumor cells that line the ductal wall, and nutrient is depleted in the tumor centers where necrotic cores form (Fig. 3), which eventually calcify. When $\theta = 30°$, the duct bulges outward into the stroma as the tumor cells proliferate. Negative pressures form near the duct wall due to resistive forces. Cells at the center of the tumor die due to lack of nutrients and then calcify due to loss of liquid volume. In the necrotic regions that have not calcified, the pressure is negative due to cell lysis. Pressure is high in the tumor center where cells have calcified and at the growing tips where cells are actively proliferating, see Fig. 4. When the cell-BM adhesion is increased, (e.g., θ increases), the tumors advance further along the duct and the leading tips become concave rather

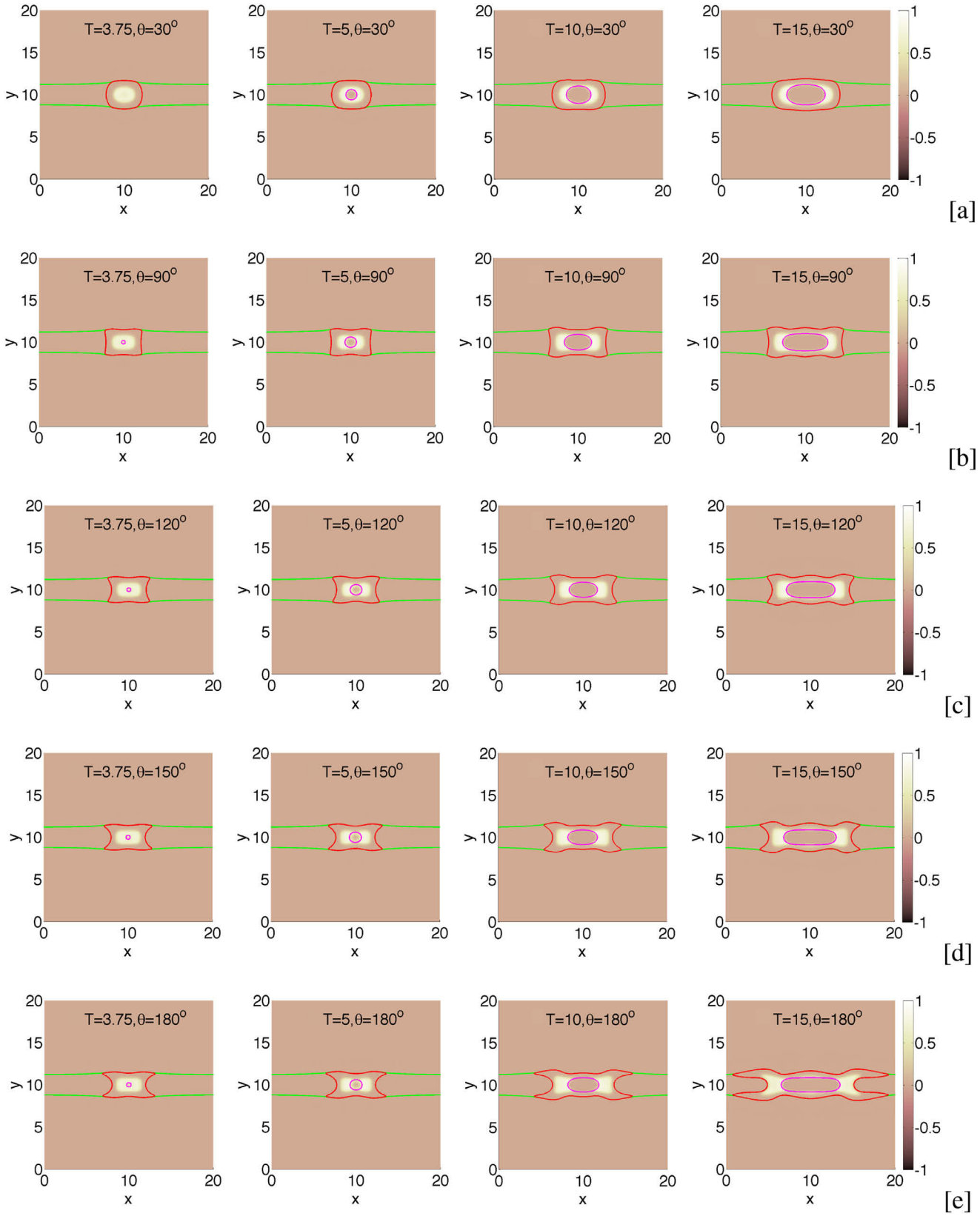

Fig. 2. Tumor cluster growth in a 2D simple duct showing the necrotic core (white regions), tumor(regions inside the red curves), microcalcification (regions inside the magenta curves), and membrane (regions inside the green curves) with different relative strengths of cell-BM adhesion as labeled via the contact angle θ. Increasing cell-membrane adhesion by increasing θ leads to larger, more elongated tumors and microcalcification. The membrane stiffness $A = 0.5$, $\gamma_c = 0.2$, and other parameters are shown in Table 1. (For interpretation of the references to colour in this figure legend, the reader is referred to the web version of this article.)

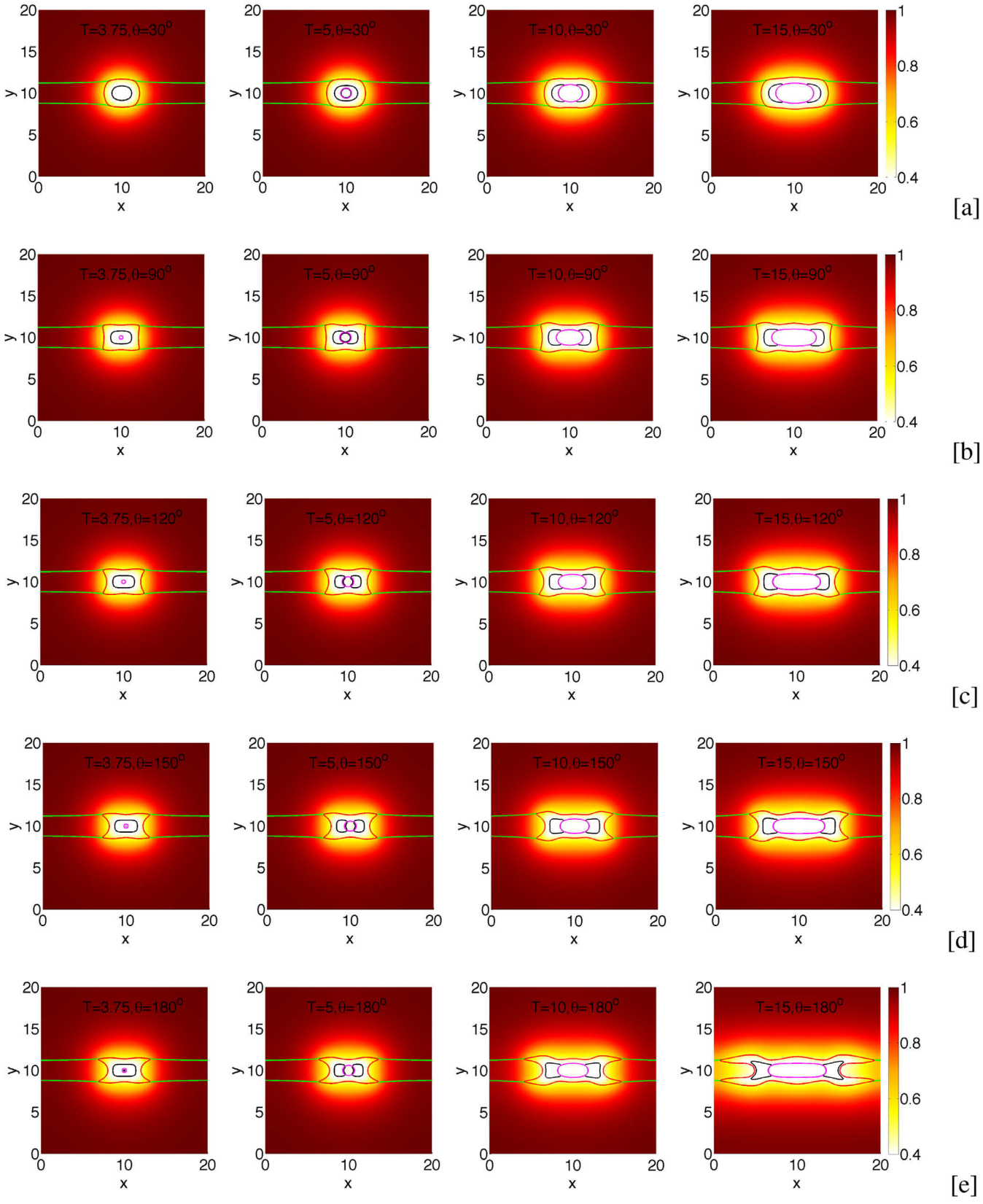

Fig. 3. The nutrient distribution of the tumor cluster growth shown in Fig. 2. Nutrient diffuses from the stroma and is uptaken by tumor cells leading to lowered nutrient concentration in the tumor interior and the development of necrotic cores (regions inside the black curves) and microcalcification (regions inside the magenta curves).

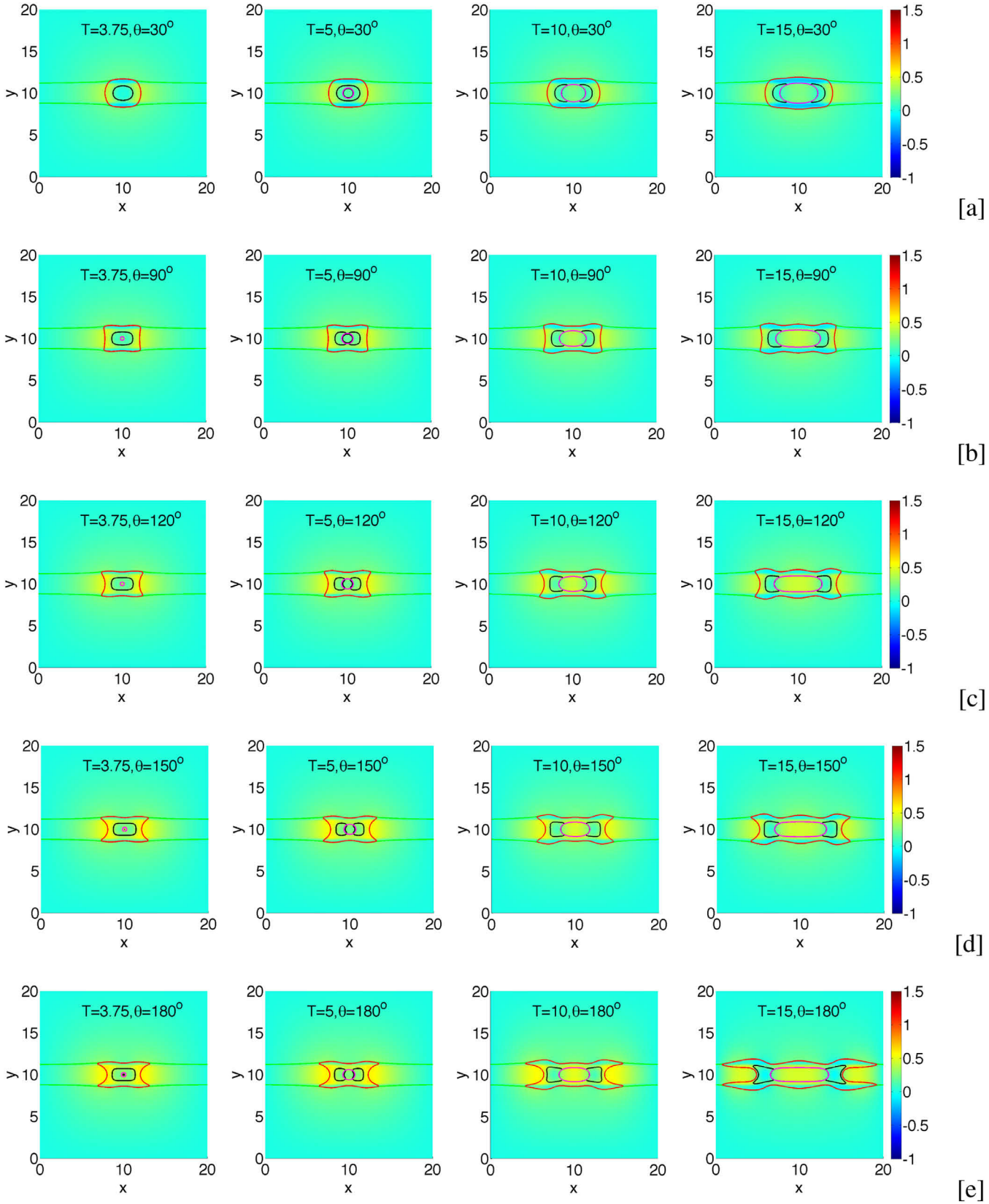

Fig. 4. The pressure profile of the tumor cluster growth shown in Fig. 2. Negative pressures form near the duct wall due to resistive forces. In the necrotic regions (regions inside the black curves) that have not calcified, the pressure is negative due to cell lysis. Pressure is high in the tumor center where cells have calcified (regions inside the magenta curves) and at the growing tips where cells are actively proliferating.

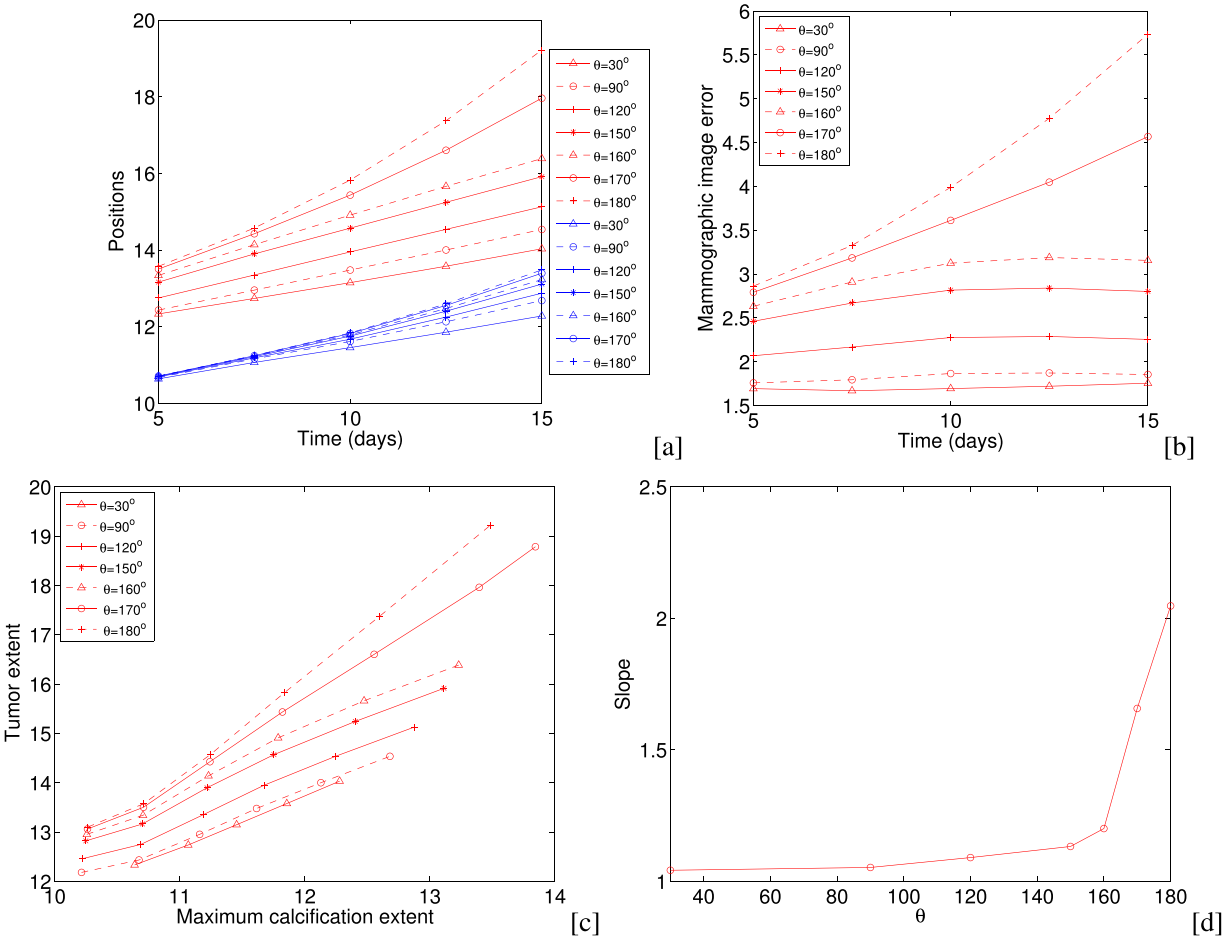

Fig. 5. (a): Tumor and microcalcification positions in the duct with different relative strengths of cell-BM adhesion as labeled via the contact angle θ. The red denotes the tumor interface and the blue denotes the boundary of the calcified region; (b): The distances between the edge of the tumor tissue and the edge of calcification with different relative strengths of cell-BM adhesion as labeled via the contact angle θ; (c): A linear correlation between the mammographic calcification and the actual pathology-measured tumor size is predicted in our simulations; (d): The slope of a linear fit between the tumor and calcification extents based on the data simulated in Fig. 2 as a function of cell-BM adhesion. (For interpretation of the references to colour in this figure legend, the reader is referred to the web version of this article.)

Table 1
Nondimensional parameters in the two dimensional numerical simulations. The computational domain is $\Omega = (0, 20) \times (0, 20)$.

ϵ	0.05	$\tilde{\epsilon}$	0.05
M	100.0	$\tilde{M}$	10.0
$\hat{M}$	60.0	$\tilde{M}$	20.0
γ	0.2	γ_C	0.2
A	0.5	ν_U	1.0
ν_p^H	0.2	ν_p^T	0.0
n_c	1.0	λ_M	1.0
λ_A	0.0	λ_N	3.0
λ_L	1.0	λ_C	0.2
λ_{LC}	0.0	n_N	0.4

than convex with the degree of concavity dependent on the cell-BM adhesion. Note that the leading edges of the calcified cells remain convex, and the leading edges of the necrotic cells stay convex for the contact angles $\theta < 150°$, but become concave at later times for large contact angles $\theta \geq 150°$. Because the tumor is more elongated along the BM, more tumor cells have access to nutrient, which results in more growth overall, see Fig. 3. We do not have direct biological evidence that ductal membranes are deformed in the way predicted by the models. However, micropapillary or cribriform DCIS tumors do not fill the ductal region. Thus the case with high cell-BM adhesion is most similar to these types of DCIS tumors. In addition, the case with low cell-BM adhesion is most consistent with solid or comedo DCIS tumors.

Because tumors (e.g., breast cancer) are detected by the calcifications that develop, the detected tumor is smaller than the actual tumor, as seen experimentally (e.g., see Leonard and Swain, 2004; de Roos et al., 2004) and in Fig. 2 presented here. However, the amount by which the tumor extends beyond the calcified cells is often hard to detect experimentally. Thus, a critical variable the mathematical model can provide is the difference between the leading edge of the tumor and the leading edge of the calcified region. Fig. 5(a) shows the leading edges of the tumor and calcified region with different relative strengths of cell-BM adhesion. The differences between those two edges are shown in Fig. 5(b). As observed experimentally (de Roos et al., 2004) and predicted by Macklin et al. (2012) that the maximum calcification diameter in mammograms and the measured pathologic tumor size have a linear correlation. Our model also predicts a linear correlation between the mammographic calcification and the actual pathology-measured tumor sizes, see Figs. 5(c) and (d). Interestingly, we find that when the leading edges of the necrotic cells become concave at later times (the case with $\theta > 150°$) the measured pathologic tumor sizes evolve much faster, see Fig. 5(d) which shows the slopes of the linear relationship between the extents of tumor and calcified cells.

Next, we investigate the effects of duct radius on tumor clusters growth and tumor microcalcification formation. We vary duct radius (denoted by small, medium and large) and cell-membrane adhesion, see Figs. 2 and 6. it is clearly seen that for fixed duct ra-

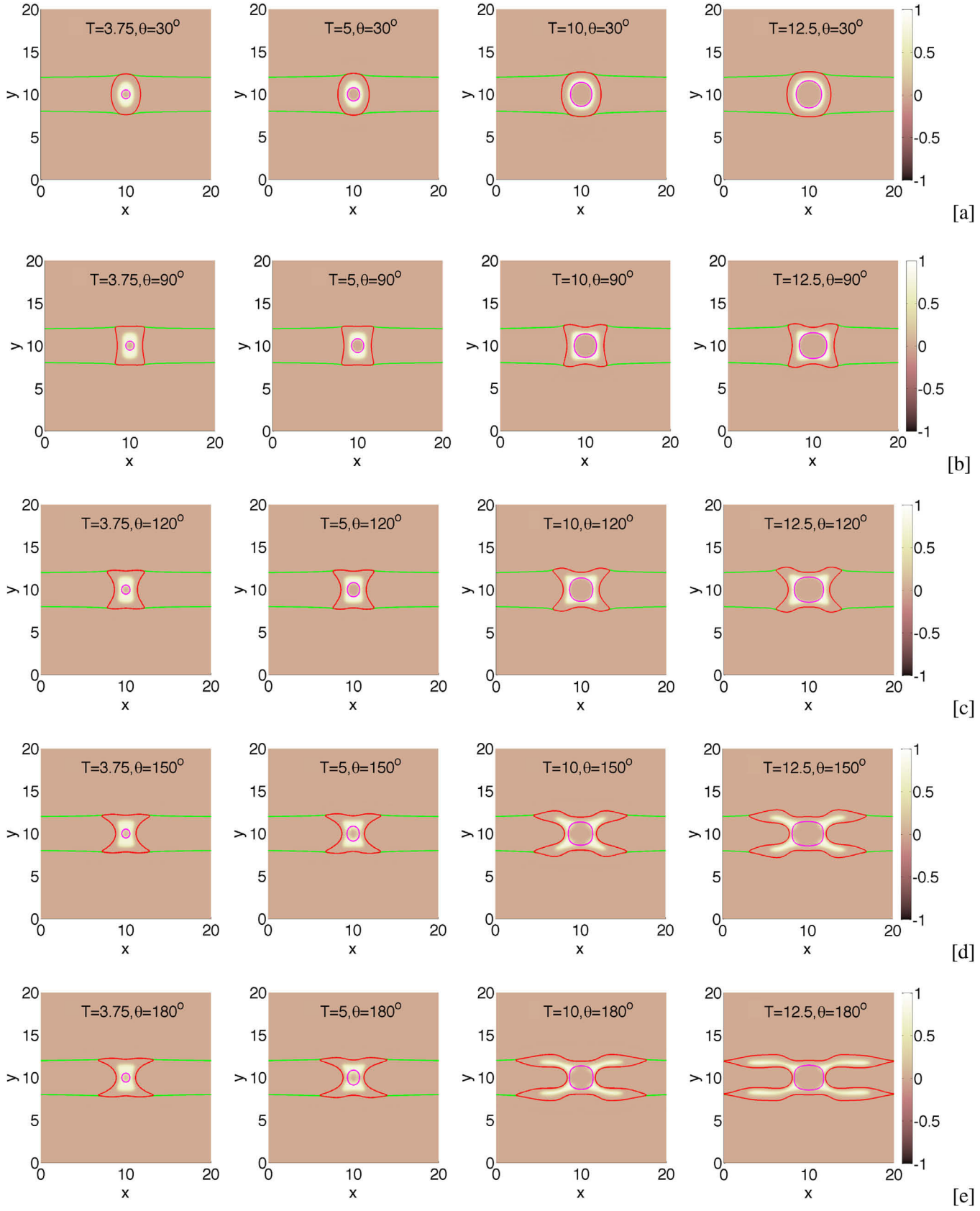

Fig. 6. Effect of enlarged duct radius on tumor clusters growth in 2D simple ducts, showing the necrotic core (white regions), tumor (regions inside the red curves), microcalcification (regions inside the magenta curves)), and membrane (regions inside the green curves)) with different cell-BM adhesion. (For interpretation of the references to colour in this figure legend, the reader is referred to the web version of this article.)

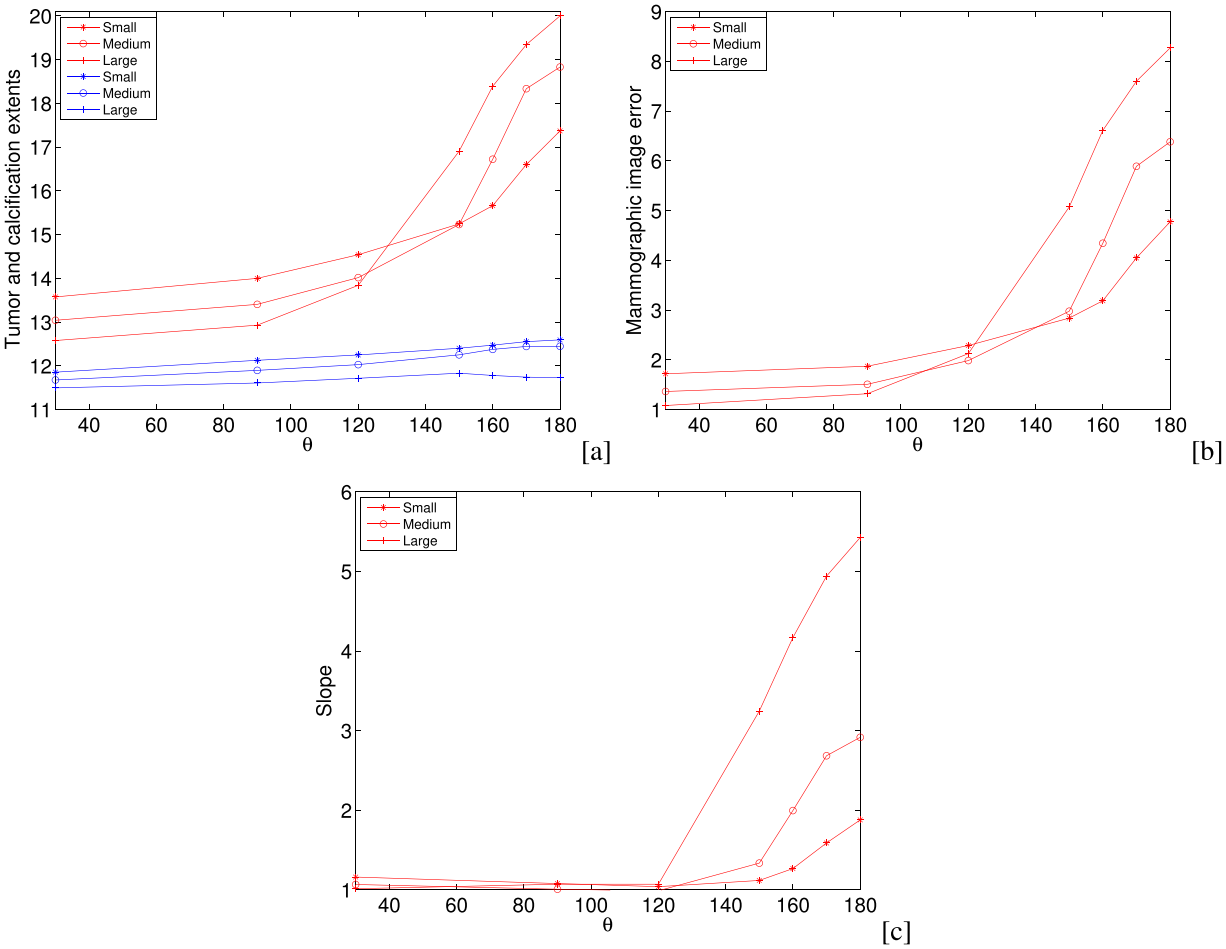

Fig. 7. (a): Tumor and microcalcification extents in the duct with different duct radius as a function of cell-BM adhesion at time $T = 12.5$. The red denotes the tumor interface and the blue denotes the boundary of the calcified region; (b): The distances between the edge of the tumor tissue and the edge of calcification with different duct radius as a function of cell-BM adhesion at time $T = 12.5$; (c): The slope of a linear fit between the tumor and calcification extents based on the data simulated in Figs. 2 and 6 as a function of cell-BM adhesion. (For interpretation of the references to colour in this figure legend, the reader is referred to the web version of this article.)

dius, tumor clusters elongate more with larger cell-membrane adhesion, which is consistent with the results we observed above. With smaller contact angle θ (e.g., $\theta \leq 90°$) tumor clusters advance faster with small duct radius, because small duct radius increases the availability of nutrients to the tumor cells. Different from smaller contact angles, Fig. 6 shows tumor clusters elongate more with larger cell-membrane contact angles in large duct, in part because the leading tips of the tumor become more concave, which is easier for nutrient to penetrate. Meanwhile, It is also clearly seen that the leading edges of the calcified cells remains convex. However, the leading edges of the necrotic cells become concave at very early times (e.g. $\theta \geq 150°$). The concavity of necrotic regions enhances the degree of concavity of the tumor tips, leading to much fast spread of the tumor tips. Our model suggests a much faster growth of the measured pathologic tumor sizes for the cases with enhanced cell-membrane adhesion. The trend can be found in Figs. 7(a) and (b). The linear correlation between the maximum calcification diameter in mammograms and the measured pathologic tumor size can be observed in Fig. 7(c). Furthermore, our model suggests a quadratic correlation between the mammographic and pathologic tumor extents with large duct radius and strong cell-BM adhesion (e.g., $\theta = 170°, 180°$). This correlation can be seen through the following quadratic fits between tumor cell (y) and calcified cell (x) extents for $\theta = 170°$:

$$y = 1.23x^2 - 22.44x + 112.9, \tag{44}$$

and $\theta = 180°$:

$$y = 1.76x^2 - 33.6x + 172.35. \tag{45}$$

Finally, we consider the effects of varying membrane stiffness A on tumor clusters progression. Characteristic tumor-BM evolutions are shown in Figs. 2 and 8 at different times with different cell-BM adhesion. Again, from Fig. 8 we see that for fixed membrane stiffness, increasing cell-membrane adhesion leads to thinner, more elongated tumors. As the stiffness, A, of the BM is increased the BM deformation is decreased and the tumor grows more compactly overall, as a result of stronger membrane restoring forces on the duct wall. Increasing membrane stiffness enhances tumor elongation along the duct. This is not the case for larger contact angle (e.g., $\theta \geq 160°$) because less stiff membrane leads to more membrane deformation, resulting in more tumor cells having access to nutrients and being able to proliferate. When the membrane stiffness is increased, the leading edges of both calcified cells and the necrotic cells remain convex for any contact angles. Tumor growth trend can be found in Figs. 9(a) and (b). The linear correlation between the maximum calcification diameter in mammograms and the measured pathologic tumor sizes can be observed in Fig. 9(c).

4. Conclusion

In this paper, we have developed a mathematical model of tumor growth and tumor microcalcification in complex, evolving geometries with elastic, deformable membranes using a diffuse

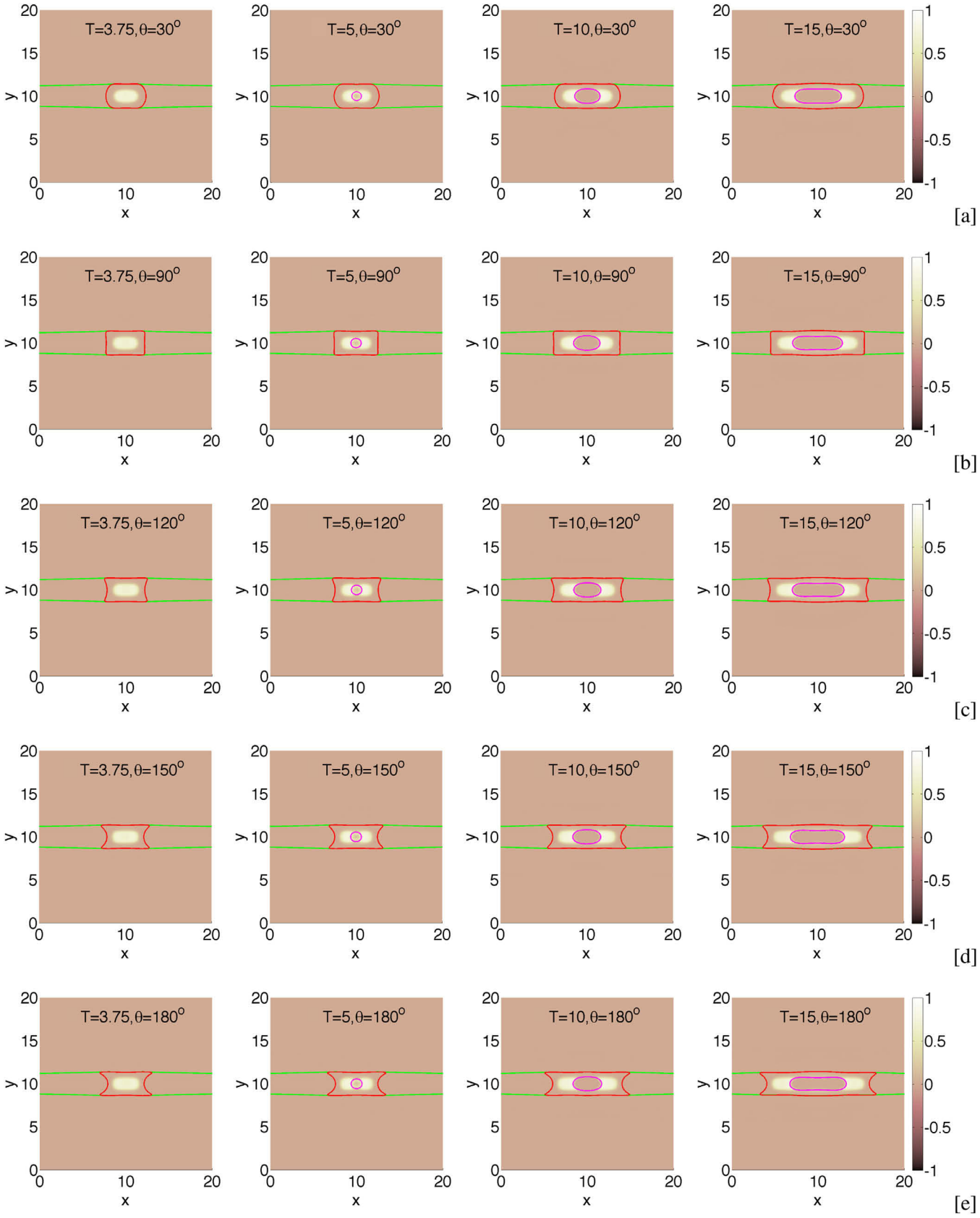

Fig. 8. Effect of increased duct wall stiffness ($A = 4.0$) on growing tumor clusters in 2D simple ducts. The tumor (regions inside the red curves), necrotic core (white regions), microcalcification (regions inside the magenta curves), and membrane (regions inside the green curves) are shown for different cell-membrane adhesion. (For interpretation of the references to colour in this figure legend, the reader is referred to the web version of this article.)

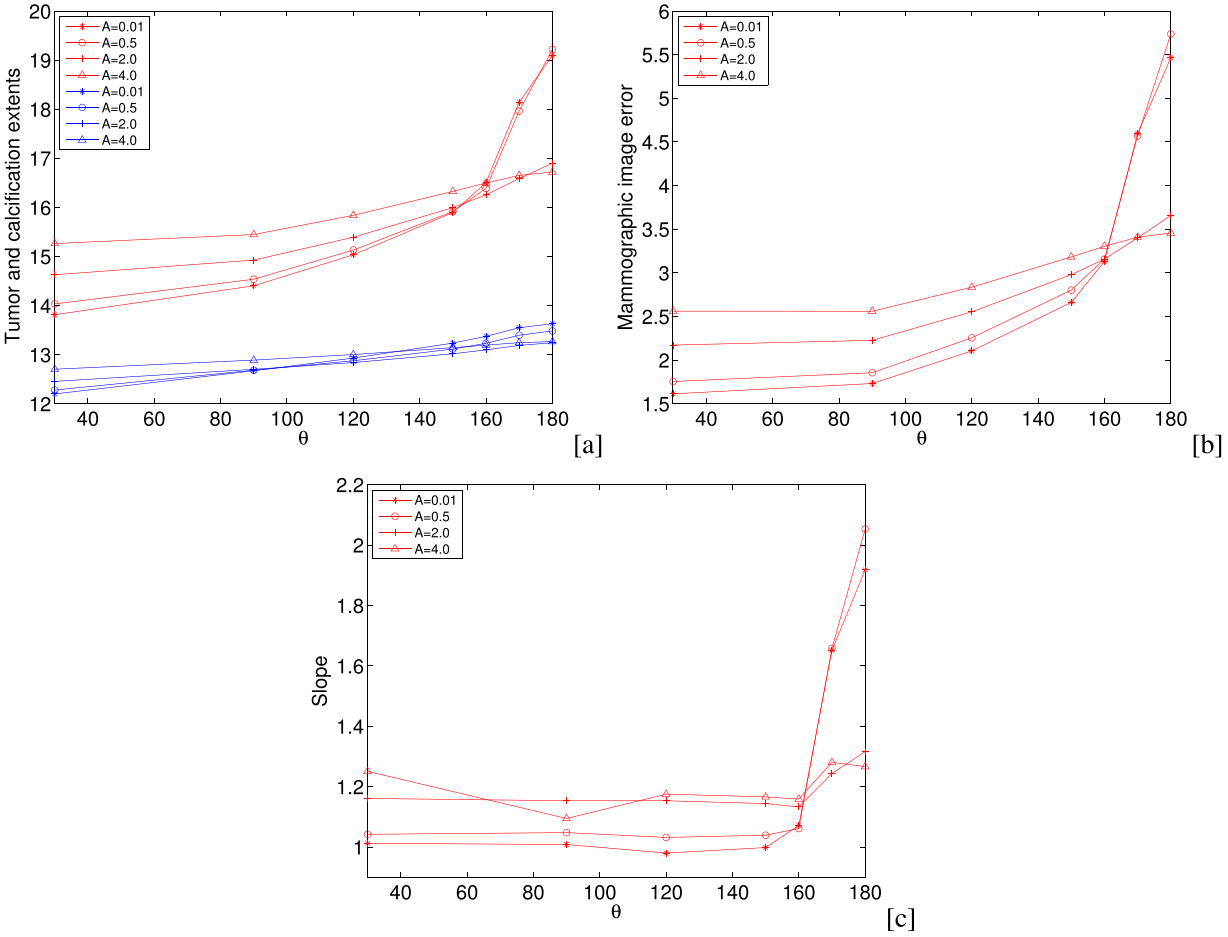

Fig. 9. (a): Tumor and microcalcification extents in the duct with different membrane stiffness as a function of cell-BM adhesion at time $T = 15$. The red denotes the tumor interface and the blue denotes the boundary of the calcified region; (b): The distances between the edge of the tumor tissue and the edge of calcification with different membrane stiffness as a function of cell-BM adhesion at time $T = 15$; [c]: The slope of a linear fit between the tumor and calcification extents based on the data simulated in Figs. 2 and 8 as a function of cell-BM adhesion. (For interpretation of the references to colour in this figure legend, the reader is referred to the web version of this article.)

domain approach (e.g., Aland et al., 2010; Chen and Lowengrub, 2014b; Li et al., 2009; Teigen et al., 2009; Teigen et al., 2011). In this methodology, the complex domain was captured implicitly using an auxiliary function and the governing equations were appropriately modified, extended and solved in a larger, regular domain. The boundary conditions appeared as singular source terms in the reformulated equations. The diffuse domain method facilitated an efficient numerical implementation that did not depend on the space dimension or on the geometry of the microenvironment. In this paper we considered very simple duct geometries, but the model can handle any microenvironmental or tumor geometry that can be represented implicitly as a level surface of a phase field function.

We applied this framework to a mixture model of tumor growth and tumor microcalcification in duct-like geometries which arise in ductal carcinoma. Besides viable and necrotic cells, we treated calcified cells as the third component of the tumor clusters. We modeled homotypic cell-cell adhesion and homotypic calcified cell-cell adhesion as well as heterotypic cell-BM adhesion with the latter being implemented via an effective contact angle between the tumor cluster and BM that arises from differences in adhesion energies through the Laplace-Young equation. We modeled the BM as an elastic membrane using a simple model of resistive forces that the membrane imparts on the tumor microenvironment. We investigated tumor progression, tumor microcalcification and BM response as a function of cell-BM adhesion, the duct size, and the stiffness of the BM. Our model suggested that tumor sizes are positively correlated with cell-BM adhesion since increasing cell-BM adhesion leads to thinner, more elongated tumors that are easier for nutrients to penetrate. From Fig. 9(a) we found that for small contact angles (e.g., $\theta \leq 150°$) tumor sizes are positively correlated with BM stiffness. However, for larger contact angles (e.g., $\theta \geq 160°$) non-monotone correlation was seen between tumor sizes and BM stiffness. Our model predicted that tumor sizes are positively correlated with duct radius for larger contact angles (e.g., $\theta > 150°$) and negatively correlated for contact angles $\leq 120°$. Clearly, there is a transition in the relationship between tumor sizes and duct radius between contact angles 120° and 150°, see Fig. 7(a). Because micropapillary or cribriform DCIS tumors do not fill the ductal region, the results with strong cell-BM adhesion are most similar to these types of DCIS tumors whereas our results with small cell-BM adhesion are most consistent with solid or comedo DCIS tumors.

The results demonstrate that enhanced membrane deformability promotes tumor growth and tumor calcification and that the mammographic and pathologic tumor sizes are linearly correlated with small duct radius or weak cell-BM adhesion as predicted by Macklin et al. (2012) using an agent-based model that does not account for the deformability of the basement membrane and the active forces that the membrane imparts on the tumor cells. However, quadratic correlations between the sizes of the mammographic and pathologic tumor clusters are predicted when the duct radius is larger and cell-BM adhesion is strong (e.g., $\theta = 170°, 180°$). While we do not have direct biological evidence that ductal membranes are deformed in the way predicted by the

models, in experiments ducts can be found showing either distorted and undistorted morphologies.

There are several ways in which the results in this paper can be extended. First, the model of BM-induced forces can be made more realistic. For example, we have recently extended the model to take into account bending forces induced by the BM using a Helfrich-like model (Du et al., 2004; Helfrich, 1973; Torabi et al., 2009 Feng et al., 2018; Chen et al., 2018). The new model is fully variational and we are able to develop an energy stable numerical scheme to solve the nonlinear system efficiently. This is the subject in a forthgoing paper. In addition, local elastic stresses can be included following the approach described in Bresch et al. (2010) and Cottet and Maitre (2004). Second, different from the tumor clusters we considered in this paper where tumors contain three components: viable cells, dead cell, and calcified cells, we can model calcified cells as a separated phase from the tumor clusters. This would help us to investigate correlations between tumor cells and calcified cells under different tumor cell and calcified cell adhesion.

Acknowledgements

YC and JL acknowledge partial funding from the National Science Foundation-Division of Mathematical Sciences (NSF grants DMS-1263796, DMS-1714973 and DMS-1763272). JL additionally acknowledges partial funding from the National Institutes of Health (NIH) through grant 1U54CA217378-01A1 for a National Center in Cancer Systems Biology at the University of California, Irvine, and NIH grant P30CA062203 for the Chao Comprehensive Cancer Center at the University of California, Irvine.

Appendix A

A stable time-discretization scheme

We discretize the nutrient equation using the centered finite difference and simply extend the stable scheme in Chen et al. (2014a) to which our problem reduces when $\psi = 1$. Let $\mathbf{u}_S^{k+1} = -\nabla p^{k+1} - \frac{\gamma}{\epsilon}\phi_T^k\psi^k\nabla\mu^{k+1} - \frac{\gamma_c}{\bar{\epsilon}}\phi_C^k\psi^k\nabla\mu_C^{k+1} + A\psi^k\nabla(\Psi^{k+1} - \psi^{k+1}) + \mathbf{v}^k$, in this way we can rewrite the equations in an equivalent form in which the velocity does not appear explicitly. Then the semi-implicit scheme for the equations is

$$\begin{aligned}
\psi^k\phi_T^{k+1} - \psi^k\phi_T^k &= s\nabla\cdot((M\psi^k\phi_T^k + \frac{\gamma}{\epsilon}(\phi_T^k)^2(\psi^k)^2)\nabla\mu^{k+1}) \\
&\quad + s\nabla\cdot(\phi_T^k\psi^k\nabla p^{k+1}) + s\nabla \\
&\quad \cdot\left(\frac{\gamma_c}{\bar{\epsilon}}\phi_T^k\phi_C^k(\psi^k)^2\nabla\mu_C^{k+1}\right) \\
&\quad - sA\nabla\cdot(\phi_T^k(\psi^k)^2\nabla(\Psi^{k+1} - \psi^{k+1})) \\
&\quad - s\nabla\cdot(\psi^k\phi_T^k\mathbf{v}^k) + s\psi^k S_T, \\
\psi^k\mu^{k+1} &= \psi^k f_c'(\phi_T^{k+1}) - \epsilon^2\nabla\cdot(\psi^k\nabla\phi_T^{k+1}) - \psi^k f_e'(\phi_T^k) \\
&\quad + \frac{\epsilon}{\sqrt{2}}\phi_T^k(1-\phi_T^k)|\nabla\psi^k|\cos\theta, \\
\psi^k\phi_D^{k+1} - \psi^k\phi_D^k &= s\nabla\cdot((\hat{M}\psi^k\phi_D^k + \frac{\gamma}{\epsilon}\phi_D^k\phi_T^k(\psi^k)^2)\nabla\mu^{k+1}) \\
&\quad + s\nabla\cdot(\phi_D^k\psi^k\nabla p^{k+1}) \\
&\quad + s\nabla\cdot(\frac{\gamma_c}{\bar{\epsilon}}\phi_D^k\phi_C^k(\psi^k)^2\nabla\mu_C^{k+1}) \\
&\quad - sA\nabla\cdot(\phi_D^k(\psi^k)^2\nabla(\Psi^{k+1} - \psi^{k+1})) \\
&\quad - s\nabla\cdot(\psi^k\phi_D^k\mathbf{v}^k) + s\psi^k S_D, \\
\psi^k\phi_C^{k+1} - \psi^k\phi_C^k &= s\nabla\cdot(\frac{\gamma}{\epsilon}\phi_T^k\phi_C^k(\psi^k)^2)\nabla\mu^{k+1}) \\
&\quad + s\nabla\cdot(\phi_C^k\psi^k\nabla p^{k+1}) \\
&\quad + s\nabla\cdot\left(\bar{M}\psi^k\phi_C^k + \frac{\gamma_c}{\bar{\epsilon}}(\phi_C^k)^2(\psi^k)^2\nabla\mu_C^{k+1}\right) \\
&\quad - sA\nabla\cdot(\phi_C^k(\psi^k)^2\nabla(\Psi^{k+1} - \psi^{k+1})) \\
&\quad - s\nabla\cdot(\psi^k\phi_C^k\mathbf{v}^k) + s\psi^k S_C, \\
\psi^k\mu_C^{k+1} &= \psi^k f_c'(\phi_C^{k+1}) - \bar{\epsilon}^2\nabla\cdot(\psi^k\nabla\phi_C^{k+1}) - \psi^k f_e'(\phi_C^k), \\
-\nabla^2 p^{k+1} &= \frac{\gamma}{\epsilon}\nabla\cdot(\phi_T^k\psi^k\nabla\mu^{k+1}) + \frac{\gamma_c}{\bar{\epsilon}}\nabla \\
&\quad \cdot(\phi_C^k\psi^k\nabla\mu_C^{k+1}) - A\nabla\cdot(\psi^k\nabla(\Psi^{k+1} - \psi^{k+1})) \\
&\quad - \nabla\cdot\mathbf{v}^k + S_T^{k+1}\frac{\psi^{k+1}}{\psi^{k+1} + \bar{\delta}}, \\
\psi^{k+1} - \psi^k &= \frac{s\gamma}{\epsilon}\nabla\cdot(\phi_T^k(\psi^k)^2\nabla\mu^{k+1}) \\
&\quad + s\nabla\cdot(\psi^k\nabla p^{k+1}) + s\nabla\cdot(\tilde{M}(\psi^k)\nabla\tilde{\mu}^{k+1}) \\
&\quad - s\psi^k\nabla^2 p^{k+1} \\
&\quad + \frac{s\gamma_c}{\bar{\epsilon}}\nabla\cdot(\phi_C^k(\psi^k)^2\nabla\mu_C^{k+1}) - \frac{s\gamma}{\epsilon}\psi^k\nabla \\
&\quad \cdot(\phi_T^k\psi^k\nabla\mu^{k+1}) - \frac{s\gamma_c}{\bar{\epsilon}}\psi^k\nabla\cdot(\phi_C^k\psi^k\nabla\mu_C^{k+1}) \\
&\quad - sA\nabla\cdot((\psi^k)^2\nabla(\Psi^{k+1} - \psi^{k+1})) \\
&\quad + sA\psi^k\nabla\cdot(\psi^k\nabla(\Psi^{k+1} - \psi^{k+1})) - s\mathbf{v}^k\cdot\nabla\psi^k, \\
\tilde{\mu}^{k+1} &= f_c'(\psi^{k+1}) - \tilde{\epsilon}^2\nabla^2\psi^{k+1} - f_e'(\psi^k),
\end{aligned}$$

where we take $S_T = \frac{S_T^k + S_T^{k+1}}{2}$, $S_D = \frac{S_D^k + S_D^{k+1}}{2}$, and s is the time step size. The nutrient concentration equation is discretized as

$$\begin{aligned}
0 &= \nabla\cdot(D(\phi_T^{k+1})\nabla n^{k+1}) \\
&\quad - n^{k+1}\big[(\phi_T^{k+1} - \phi_D^{k+1})\psi^k + \nu_p^H(1 - Q(\psi^{k+1}\phi_T^{k+1})) \\
&\quad + \nu_p^T Q(\psi^{k+1}\phi_T^{k+1})\big] \\
&\quad + n_c(\nu_p^H(1 - Q(\psi^{k+1}\phi_T^{k+1})) + \nu_p^T Q(\psi^{k+1}\phi_T^{k+1})).
\end{aligned}$$

Finite difference discretization

Here we assume that the computational domain Ω^s is rectangular, i.e., $\Omega^s = (0, N_x h)\times(0, N_y h)$, where N_x and N_y are positive integers, and $h > 0$ is the spatial step size. Define $x_i = (i - 1/2)h$ and $y_i = (i - 1/2)h$, where i is an integer or half integer. Consider the following three set of uniform grid points: (i) east-west edge points E^{ew}, (ii) north-south edge points E^{ns}, (iii) cell-centered points C, defined via

$$\begin{aligned}
E^{ew} &= \{(x_{i+\frac{1}{2}}, y_j)|i = 0,\cdots,N_x, j = 1,\cdots,N_y\}, \\
E^{ns} &= \{(x_i, y_{j+\frac{1}{2}})|i = 1,\cdots,N_x, j = 0,\cdots,N_y\}, \\
C &= \{(x_i, y_j)|i = 0,\cdots,N_x+1, j = 0,\cdots,N_y+1\}.
\end{aligned}$$

Real-valued grid functions whose domains equal E^{ew} are called east-west edge-centered functions and are identified via $f_{i+\frac{1}{2},j} = f(x_{i+\frac{1}{2}}, y_j)$; those whose domains equal E^{ns} are called north-south edge-centered functions and are identified via $f_{i,j+\frac{1}{2}} = f(x_i, y_{j+\frac{1}{2}})$; and those whose domains equal C are called cell-centered functions and are identified via $\phi_{i,j} = \phi(x_i, y_j)$. The velocities $\mathbf{v}$ is approximated as edge-centered functions. For example, writing $\mathbf{v} = (v^{ew}, v^{ns})$, v^{ew} is approximated as an east-west edge-centered function, and v^{ns} is approximated as a north-south edge-centered function. All other dependent variable are approximated as cell-centered functions.

To complete the spatial discretization, we replace spatial derivatives by difference operators. The Laplacian operator is approximated to second order by

$$\nabla_d^2\phi_{i,j} = \frac{\phi_{i+1,j} + \phi_{i-1,j} + \phi_{i,j+1} + \phi_{i,j-1} - 4\phi_{i,j}}{h^2},$$

where ϕ is cell-centered. The Laplacian with non-constant diffusivity/mobility is approximated to second order via

$$\nabla_d \cdot (m\nabla_d\phi)_{i,j} = \frac{A_x m_{i+\frac{1}{2},j}(\phi_{i+1,j}-\phi_{i,j}) - A_x m_{i-\frac{1}{2},j}(\phi_{i,j}-\phi_{i-1,j})}{h^2} + \frac{A_y m_{i,j+\frac{1}{2}}(\phi_{i,j+1}-\phi_{i,j}) - A_y m_{i,j-\frac{1}{2}}(\phi_{i,j}-\phi_{i,j-1})}{h^2},$$

where both ϕ and m are assumed to be cell-centered, and A_x and A_y are the averaging operators defined component-wise as

$$A_x m_{i+\frac{1}{2},j} = \frac{m_{i+1,j}+m_{i,j}}{2}, \qquad A_x m_{i-\frac{1}{2},j} = \frac{m_{i,j}+m_{i-1,j}}{2},$$
$$A_y m_{i,j+\frac{1}{2}} = \frac{m_{i,j+1}+m_{i,j}}{2}, \qquad A_y m_{i,j-\frac{1}{2}} = \frac{m_{i,j}+m_{i,j-1}}{2}.$$

To calculate the advection term $\nabla\cdot(\mathbf{v}\phi)$, where ϕ is cell-centered and $\mathbf{v}$ is the edge-centered cell velocity, we use the third-order WENO reconstruction method (Jiang and Shu, 1996), with the simple upwind flux. In particular, we approximate $\nabla\cdot(\mathbf{v}\phi)$ by

$$\nabla_d\cdot(\mathbf{v}\phi)_{i,j} = \nabla_d\cdot\mathbf{f}_{i,j} = \frac{f^{ew}_{i+\frac{1}{2},j} - f^{ew}_{i-\frac{1}{2},j}}{h} + \frac{f^{ns}_{i,j+\frac{1}{2}} - f^{ns}_{i,j-\frac{1}{2}}}{h}.$$

The field $\mathbf{f} = (f^{ew}, f^{ns})$ is the numerical upwind flux and is determined by

$$f^{ew}_{i+\frac{1}{2},j} = v^{ew}_{i+\frac{1}{2},j} W^{ew}_{i+\frac{1}{2},j}(\phi),$$
$$f^{ns}_{i,j+\frac{1}{2}} = v^{ns}_{i,j+\frac{1}{2}} W^{ns}_{i,j+\frac{1}{2}}(\phi),$$

where $W^{ew}_{i+\frac{1}{2},j}(\phi)$ is the upwind WENO reconstruction of ϕ to the east-west cell edges, and $W^{ns}_{i,j+\frac{1}{2}}(\phi)$ is the upwind WENO reconstruction of ϕ to the north-south cell edges.

The fully discrete stable scheme is thus given by

$$\begin{aligned}
\psi^k_{i,j}\phi^{k+1}_{T_{i,j}} - \psi^k_{i,j}\phi^k_{T_{i,j}} &= s\nabla_d\cdot((M\psi^k\phi^k_T + \frac{\gamma}{\epsilon}(\phi^k_T)^2(\psi^k)^2)\nabla_d\mu^{k+1})_{i,j} \\
&+ s\nabla_d\cdot(\phi^k_T\psi^k\nabla d p^{k+1})_{i,j} \\
&+ s\nabla_d\cdot\left(\frac{\gamma_c}{\bar\epsilon}\phi^k_T\phi^k_C(\psi^k)^2\nabla_d\mu^{k+1}_C\right)_{i,j} \\
&- sA\nabla_d\cdot(\phi^k_T(\psi^k)^2\nabla_d(\Psi^{k+1}-\psi^{k+1}))_{i,j} \\
&- s\nabla_d\cdot(\psi^k\phi^k_T\mathbf{v}^k)_{i,j} + s\psi^k_{i,j}S_{T_{i,j}}, \\
\psi^k_{i,j}\mu^{k+1}_{i,j} &= \psi^k_{i,j}f_c'(\phi^{k+1}_{T_{i,j}}) - \epsilon^2\nabla_d\cdot(\psi^k\nabla_d\phi^{k+1}_T)_{i,j} \\
&- \psi^k_{i,j}f_e'(\phi^k_{T_{i,j}}) \\
&+ \frac{\epsilon}{\sqrt{2}}\phi^k_{T_{i,j}}(1-\phi^k_{T_{i,j}})|\nabla_d\psi^k_{i,j}|\cos\theta,\ \psi^k_{i,j}\phi^{k+1}_{D_{i,j}} \\
&- \psi^k_{i,j}\phi^k_{D_{i,j}} = s\nabla_d \\
&\cdot\left((M\psi^k\phi^k_D + \frac{\gamma}{\epsilon}\phi^k_D\phi^k_T(\psi^k)^2)\nabla_d\mu^{k+1}\right)_{i,j} \\
&+ s\nabla_d\cdot(\phi^k_D\psi^k\nabla_d p^{k+1})_{i,j} \\
&+ s\nabla_d\cdot\left(\frac{\gamma_c}{\bar\epsilon}\phi^k_D\phi^k_C(\psi^k)^2\nabla_d\mu^{k+1}_C\right)_{i,j} \\
&- sA\nabla_d\cdot\left(\phi^k_D(\psi^k)^2\nabla_d(\Psi^{k+1}-\psi^{k+1})\right)_{i,j} \\
&- s\nabla_d\cdot(\psi^k\phi^k_D\mathbf{v}^k)_{i,j} + s\psi^k_{i,j}S_{D_{i,j}}, \\
\psi^k_{i,j}\phi^{k+1}_{C_{i,j}} - \psi^k_{i,j}\phi^k_{C_{i,j}} &= s\nabla_d\cdot\left(\frac{\gamma}{\epsilon}\phi^k_T\phi^k_C(\psi^k)^2\right)\nabla_d\mu^{k+1})_{i,j} \\
&+ s\nabla_d\cdot(\phi^k_C\psi^k\nabla p^{k+1})_{i,j} + s\nabla_d \\
&\cdot(\bar M\psi^k\phi^k_C + \frac{\gamma_c}{\bar\epsilon}(\phi^k_C)^2(\psi^k)^2\nabla_d\mu^{k+1}_C)_{i,j} \\
&- sA\nabla_d\cdot(\phi^k_C(\psi^k)^2\nabla_d(\Psi^{k+1} \\
&- \psi^{k+1}))_{i,j} - s\nabla_d\cdot(\psi^k\phi^k_C\mathbf{v}^k)_{i,j} + s\psi^k_{i,j}S_{C_{i,j}},
\end{aligned}$$

$$\begin{aligned}
\psi^k_{i,j}\mu^{k+1}_{C_{i,j}} &= \psi^k_{i,j}f_c'(\phi^{k+1}_{C_{i,j}}) - \bar\epsilon^2\nabla_d\cdot(\psi^k\nabla\phi^{k+1}_C)_{i,j} \\
&- \psi^k f_e'(\phi^k_{C_{i,j}}), \\
-\nabla^2 p^{k+1}_{i,j} &= \frac{\gamma}{\epsilon}\nabla_d\cdot(\phi^k_T\psi^k\nabla_d\mu^{k+1})_{i,j} \\
&+ \frac{\gamma_c}{\bar\epsilon}\nabla_d\cdot(\phi^k_C\psi^k\nabla_d\mu^{k+1}_C)_{i,j} \\
&+ A\nabla_d\cdot(\psi^k\nabla_d(\Psi^{k+1}-\psi^{k+1}))_{i,j} \\
&- \nabla_d\cdot\mathbf{v}_{\mathbf{i},\mathbf{j}}{}^k + S^{k+1}_{T_{i,j}}\frac{\psi^{k+1}_{i,j}}{\psi^{k+1}_{i,j}+\tilde\delta}, \\
\psi^{k+1}_{i,j} - \psi^k_{i,j} &= \frac{s\gamma}{\epsilon}\nabla_d\cdot(\phi^k_T(\psi^k)^2\nabla_d\mu^{k+1})_{i,j} \\
&+ s\nabla_d\cdot(\psi^k\nabla_d p^{k+1})_{i,j} \\
&+ \frac{s\gamma_c}{\bar\epsilon}\nabla_d\cdot(\phi^k_C(\psi^k)^2\nabla_d\mu^{k+1}_C)_{i,j} \\
&+ s\nabla_d\cdot(\tilde M(\psi^k)\nabla_d\tilde\mu^{k+1})_{i,j} - s\psi^k_{i,j}\nabla^2_d p^{k+1}_{i,j} \\
&- \frac{s\gamma}{\epsilon}\psi^k_{i,j}\nabla_d\cdot(\phi^k_T\psi^k\nabla_d\mu^{k+1})_{i,j} \\
&- \frac{s\gamma_c}{\bar\epsilon}\psi^k_{i,j}\nabla_d\cdot(\phi^k_C\psi^k\nabla_d\mu^{k+1}_C)_{i,j} \\
&- sA\nabla_d\cdot((\psi^k)^2\nabla_d(\Psi^{k+1}-\psi^{k+1}))_{i,j} \\
&+ sA\psi^k_{i,j}\nabla_d\cdot(\psi^k\nabla_d(\Psi^{k+1}-\psi^{k+1}))_{i,j} \\
&- s\mathbf{v}^k_{i,j}\cdot\nabla_d\psi^k_{i,j}, \\
\tilde\mu^{k+1}_{i,j} &= f_c'(\psi^{k+1}_{i,j}) - \tilde\epsilon^2\nabla^2_d\psi^{k+1}_{i,j} - f_e'(\psi^k_{i,j}),
\end{aligned}$$

and

$$\begin{aligned}
0 = \nabla_d\cdot(D(\phi^{k+1}_T)\nabla_d n^{k+1})_{i,j} - n^{k+1}_{i,j}\Big[&(\phi^{k+1}_{T_{i,j}} - \phi^{k+1}_{D_{i,j}})\psi^k_{i,j} \\
&+\nu^H_p(1-Q(\psi^{k+1}_{i,j}\phi^{k+1}_{T_{i,j}})) + \nu^T_p Q(\psi^{k+1}_{i,j}\phi^{k+1}_{T_{i,j}})\Big] \\
&+(n_c)_{i,j}\Big(\nu^H_p(1-Q(\psi^{k+1}_{i,j}\phi^{k+1}_{T_{i,j}})) + \nu^T_p Q(\psi^{k+1}_{i,j}\phi^{k+1}_{T_{i,j}})\Big).
\end{aligned}$$

To solve the fully coupled, nonlinear system of equations at the implicit time step, we use a nonlinear multigrid method (Trottenberg et al., 2001). We refer the reader to Chen and Lowengrub (2014b); Chen et al. (2014a) and Chen (2012) for more details of the algorithm.

References

Aland, S., Egerer, S., Lowengrub, J., Voigt, A., 2014. Diffuse interface models of locally inextensible vesicles in a viscous fluid. J. Comput. Phys. 277, 32–47.

Aland, S., Lowengrub, J., Voigt, A., 2010. Two-phase flow in complex geometries: a diffuse domain approach. CMES 57, 77–106.

Bresch, D., Colin, T., Grenier, E., Ribba, B., Saut, O., 2010. Copmutational modeling of solid tumor growth: the avascular stage. SIAM J. Sci. Comput. 32 (4), 2321–2344.

Byrne, H.M., Chaplain, M.A.J., 1995. Growth of non necrotic tumors in the presence and absence of inhibitors. Math. Biosci. 130, 151–181.

Chapa, J., Bourgo, R.J., Greene, G.L., Kulkarni, S., An, G., 2013. Examining the pathogenesis of breast cancer using a novel agent-based model of mammary ductal epithelium dynamics. PLoS ONE 8 (5). E64091

Chen, Y., 2012 Ph.d. thesis. University of California at Irvine

Chen, Y., Lowengrub, J.S., 2014b. Tumor growth in complex, evolving microenvironmental geometries: i. a diffuse domain approach. J. Theor. Biol. 361, 14–30.

Chen, Y., Wise, S.M., Shenoy, V., Lowengrub, J., 2014a. A stable scheme for a nonlinear, multiphase tumor growth model with an elastic membrane. Int. J. Numer. Meth. Biomed. Eng. 30, 726–754.

Chen, Y., Lowengrub, J., Shen, J., Wang, C., Wise, S., 2018. Efficient energy stable schemes for isotropic and strongly anisotropic Cahn–Hilliard systems with the Willmore regularization. J. Comput. Phys. 361, 56–73.

Cottet, G.H., Maitre, E., 2004. A level-set formulation of immersed boundary methods for fluid-structure interaction problems. C.R. Acad. Sci. Paris, Ser. I 338, 581–586.

Dillon, R., Owen, M., Painter, K., 2008. A Single-cell Based Model of Multicellular Growth Using the Immersed Boundary Method. In: Khoo, B.C., Li, Z., Lin, P. (Eds.), Contemporary Mathematics: Moving Interface Problems and Applications in Fluid Dynamics, Vol. 466, pp. 1–15. AMS, Providence. ISBN 978-0-8218-4267-6 (Chapter 1)

Do-Quang, M., Amberg, G., 2010. Numerical simulation of the coupling problems of a solid sphere impacting on a liquid free surface. Math. Comp. Sim. 80, 1664–1673.
Du, Q., Liu, C., Wang, X., 2004. A phase field approach in the numerical study of bending energy for vesicle membranes. J. Comput. Phys. 198, 450–468.
Erbas, B., Provenzano, E., Armes, J., Gertig, D., 2006. The natural history of ductal carcinoma in situ of the breast: a review. Breast Cancer Res. Treat. 97 (2), 135–144.
Franks, S.J., Byrne, H.M., King, J.R., Underwood, J.C.E., Lewis, C.E., 2003a. Modelling the early growth of ductal carcinoma in situ of the breast. J. Math. Biol. 47 (5), 424–452.
Feng, W., Guan, Z., Lowengrub, J., Wang, C., Chen, Y., 2018. A uniquely solvable, energy stable numerical scheme for the Functionalized Cahn–Hilliard equation and its convergence analysis. J. Sci. Comput. 76 (3), 1938–1967.
Franks, S.J., Byrne, H.M., Mudhar, H., Underwood, J.C.E., Lewis, C.E., 2003b. Modelling the growth of comedo ductal carcinoma in situ. Math. Med. Biol. 20 (3), 277–308.
Franks, S.J., Byrne, H.M., Underwood, J.C.E., Lewis, C.E., 2005. Biological inferences from a mathematical model of comedo ductal carcinoma in situ of the breast. J. Theor. Biol. 232 (4), 523–543.
Gatenby, R.A., Smallbone, K., Maini, P.K., Rose, F., Averill, J., Nagle, R.B., Eorrall, L., Gillies, R.J., 2007. Cellular adaptations to hypoxia and acidosis during somatic evolution of breast cancer. Br. J. Cancer 97 (5), 646–653.
Granasy, L., Pusztai, T., Saylor, D., Warren, J.A., 2007. Phase field theory of heterogeneous crystal nucleation. Phys. Rev. Lett. 98, 035703.
Helfrich, W., 1973. Elastic properties of lipid bilayers- theory and possible experiments. Zeitschrift für Naturforschung C. 28, 693–703.
Jacqmin, D., 1999. Calculation of two-phase navier-stokes flows using phase-field modeling. J. Comput. Phys. 155, 96–127.
Jiang, G.S., Shu, C.W., 1996. Efficient implementation of weighted ENO schemes. J. Comput. Phys. 126, 202–228.
Kerlikowske, K., Molinaro, A., Cha, I., Ljung, B.M., Ernster, V.L., Stewart, K., Chew, K., Moore II, D.H., Waldman, F., 2003. Characteristics associated with recurrence among women with ductal carcinoma in situ treated by lumpectomy. J. Natl. Cancer Inst. 95 (22), 1692–1702.
Kim, Y., Othmer, H.G., 2013. A hybrid model of tumor-stromal interactions in breast cancer. Bull. Math. Biol. doi:10.1007/s11538-012-9787-0.
Leonard, G.D., Swain, S.M., 2004. Ductal carcinoma in situ, complexities and challenges. J. Nat. Cancer Ins. 96 (12), 906–920.
Li, X., Lowengrub, J., Räez, A., Voigt, A., 2009. Solving PDEs in complex geometries: a diffusion domain approach. Commun. Math. Sci. 7, 81–107.
Macklin, P., Edgerton, M.E., Thompson, A.M., Cristini, V., 2012. Patient-calibrated agent-based modelling of ductal carcinoma in situ (DCIS): from microscopic measurements to macroscopic predictions of clinical progression. J. Theor. Biol. 301, 122–140.
Lowengrub, J., Truskinovsky, L., 1998. Quasi-incompressible Cahn-Hilliard fluids and topological transitions. Proc. R. Soc. Lond. A Math. Phys. Eng. Sci. 454, 2617–2654.
Norton, K.A., Wininger, M., Bhanot, G., Ganesan, S., Barnard, N., Shinbrot, T., 2010. A 2d mechanistic model of breast ductal carcinoma in situ (DCIS) morphology and progression. J. Theor. Biol. 263 (4), 393–406.
Page, D.L., Dupont, W.D., Rogers, L.W., Landenberger, M., 1982. Intraductal carcinoma of the breast: follow-up after biopsy only. Cancer 49 (4), 751–758.
Panorchan, P., Thompson, M.S., Davis, K.J., Tseng, Y., Konstantopoulos, K., Wirtz, D., 2006. Single-molecule analysis of cadherin-mediated cell?cell adhesion. J. Cell Sci. 119 (1), 66–74.
Pego, R., 1989. Front migration in the nonlinear cahn-hilliard equation. Proc. R. Soc. Lond. A 422, 261–278.
Rejniak, K.A., 2007a. An immersed boundary framework for modeling the growth of individual cells: an application to the early tumour development. J. Theor. Biol. 247 (1), 186–204.
Rejniak, K.A., Anderson, A.R.A., 2008a. A computational study of the development of epithelial acini: i. sufficient conditions for the formation of a hollow structure. Bull. Math. Biol. 70 (3), 677–712.
Rejniak, K.A., Anderson, A.R.A., 2008b. A computational study of the development of epithelial acini: II. necessary conditions for structure and lumen stability. Bull. Math. Biol. 70 (5), 1450–1479.
Rejniak, K.A., Dillon, R.H., 2007b. A single cell-based model of the ductal tumor microarchitecture. Comp. Math. Meth. Med. 8 (1), 51–69.
de Roos, M.A., Pijnappel, R.M., Post, W.J., de Vries, J., Baas, P.C., Groote, L.D., 2004. Correlation between imaging and pathology in ductal carcinoma in situ of the breast. World J. Surg. Oncol. 2 (4).
Sakorafas, G.H., Tsiotou, A.G.H., 2000. Ductal carcinoma in situ (DCIS) of the breast: evolving perspectives. Cancer Treat. Rev. 26, 103–125.
Sanders, M.E., Schuyler, P.A., Dupont, W.D., Page, D.L., 2005. The natural history of low-grade ductal carcinoma in situ of the breast in women treated by biopsy only revealed over 30 years of long-term follow-up. Cancer 103 (2), 2481–2484.
Silva, A.S., Gatenby, R.A., Gillies, R.J., Yunes, J.A., 2010. A quantitative theoretical model for the development of malignancy in ductal carcinoma in situ. J. Theor. Biol. 262 (4), 601–613.
Smallbone, K., Gatenby, R.A., Gillies, R.J., Maini, P.K., Gavaghan, D.J., 2007. Metabolic changes during carcinogenesis: potential impact on invasiveness. J. Theor. Biol. 244 (2), 703–713.
Teigen, K.E., Li, X., Lowengrub, J., Wang, F., Voigt, A., 2009. A diffuse-interface approach for modelling transport, diffusion and adsorption/desorption of material quantities on a deformable interface. Commun. Math. Sci. 7, 1009–1037.
Teigen, K.E., Song, P., Lowengrub, J., Voigt, A., 2011. A diffusion-interface method for two-phase flows with soluble surfactants. J. Comput. Phys. 230, 375–393.
Thomas, A., 2017. A general mixture model for nonlinear heterogeneous tumor growth. University of California, Irvine.
Torabi, S., Lowengrub, J., Voigt, A., Wise, S.M., 2009. A new phase field model for strongly anisotropic systems. Proc. R. Soc. A 465, 1337–1359.
Trottenberg, U., Oosterlee, C., Schüller, A., 2001. Multigrid. Academic Press, New York.
Venkatesan, A., Chu, P., Kerlikowske, K., Sickles, E.A., Smith-Bindman, R., 2009. Positive predictive value of specific mammographic findings according to reader and patient variables. Radiology 250 (3), 648–657.
Wise, S.M., Lowengrub, J.S., Frieboes, H.B., Cristini, V., 2008. Three-dimensional multispecies nonlinear tumor growth–i: model and numerical method. J. Theor. Biol. 253, 524–543.
Wise, S., Lowengrub, J., Cristini, C., 2011. An adaptive multigrid algorithm for simulating solid tumor growth using mixture models. Math. Comput. Modeling 53, 1–20.
Xu, Y., 2004. A free boundary problem model of ductal carcinoma in situ. Discrete Contin. Dyn. Syst. 4, 337–348.